A&A 594, A39 (2016)
DOI: 10.1051/0004-6361/201628337

Astronomy & Astrophysics

Activity indicators and stellar parameters of the *Kepler* targets

An application of the ROTFIT pipeline to LAMOST-*Kepler* stellar spectra[⋆,⋆⋆]

A. Frasca[1], J. Molenda-Żakowicz[2,3], P. De Cat[4], G. Catanzaro[1], J. N. Fu[5], A. B. Ren[5], A. L. Luo[6], J. R. Shi[6], Y. Wu[6], and H. T. Zhang[6]

[1] INAF–Osservatorio Astrofisico di Catania, via S. Sofia, 78, 95123 Catania, Italy
e-mail: antonio.frasca@oact.inaf.it
[2] Astronomical Institute of the University of Wrocław, ul. Kopernika 11, 51-622 Wrocław, Poland
[3] Department of Astronomy, New Mexico State University, Las Cruces, NM 88003, USA
[4] Royal observatory of Belgium, Ringlaan 3, 1180 Brussel, Belgium
[5] Department of Astronomy, Beijing Normal University, 19 Avenue Xinjiekouwai, 100875 Beijing, PR China
[6] Key Lab for Optical Astronomy, National Astronomical Observatories, Chinese Academy of Sciences, 100012 Beijing, PR China

Received 18 February 2016 / Accepted 23 June 2016

ABSTRACT

Aims. A comprehensive and homogeneous determination of stellar parameters for the stars observed by the *Kepler* space telescope is necessary for statistical studies of their properties. As a result of the large number of stars monitored by *Kepler*, the largest and more complete databases of stellar parameters published to date are multiband photometric surveys. The LAMOST-*Kepler* survey, whose spectra are analyzed in the present paper, was the first large spectroscopic project, which started in 2011 and aimed at filling that gap. In this work we present the results of our analysis, which is focused on selecting spectra with emission lines and chromospherically active stars by means of the spectral subtraction of inactive templates. The spectroscopic determination of the atmospheric parameters for a large number of stars is a by-product of our analysis.

Methods. We have used a purposely developed version of the code ROTFIT for the determination of the stellar parameters by exploiting a wide and homogeneous collection of real star spectra, namely the Indo US library. We provide a catalog with the atmospheric parameters ($T_{\rm eff}$, $\log g$, and [Fe/H]), radial velocity (RV), and an estimate of the projected rotation velocity ($v \sin i$). For cool stars ($T_{\rm eff} \leq 6000$ K), we also calculated the Hα and Ca II-IRT fluxes, which are important proxies of chromospheric activity.

Results. We have derived the RV and atmospheric parameters for 61 753 spectra of 51 385 stars. The average uncertainties, which we estimate from the stars observed more than once, are about 12 km s^{-1}, 1.3%, 0.05 dex, and 0.06 dex for RV, $T_{\rm eff}$, $\log g$, and [Fe/H], respectively, although they are larger for the spectra with a very low signal-to-noise ratio. Literature data for a few hundred stars (mainly from high-resolution spectroscopy) were used to peform quality control of our results. The final accuracy of the RV is about 14 km s^{-1}. The accuracy of the $T_{\rm eff}$, $\log g$, and [Fe/H] measurements is about 3.5%, 0.3 dex, and 0.2 dex, respectively. However, while the $T_{\rm eff}$ values are in very good agreement with the literature, we noted some issues with the determination of [Fe/H] of metal poor stars and the tendency, for $\log g$, to cluster around the values typical for main-sequence and red giant stars. We propose correction relations based on these comparisons and we show that this does not have a significant effect on the determination of the chromospheric fluxes. The RV distribution is asymmetric and shows an excess of stars with negative RVs that are larger at low metallicities. Despite the rather low LAMOST resolution, we were able to identify interesting and peculiar objects, such as stars with variable RV, ultrafast rotators, and emission-line objects. Based on the Hα and Ca II-IRT fluxes, we found 442 chromospherically active stars, one of which is a likely accreting object. The availability of precise rotation periods from the *Kepler* photometry allowed us to study the dependency of these chromospheric fluxes on the rotation rate for a very large sample of field stars.

Key words. surveys – techniques: spectroscopic – stars: fundamental parameters – stars: kinematics and dynamics – stars: activity – stars: chromospheres

1. Introduction

Large databases of astronomical observations have been constructed since the dawn of astronomy. Even though the content of the early catalogs was relatively simple and the observations reported there suffered from low precision and various systematic errors, careful analysis of those data led to discoveries that are now considered to be milestones in our understanding of the structure and evolution of the Universe (see, e.g., Kepler 1609; Shapley & Curtis 1921; Hubble 1942).

Also in modern astronomy, projects like Optical Gravitational Lensing Experiment (OGLE; Udalski et al. 1992), All Sky Automated Survey (ASAS; Pojmański 1997), Sloan Digital Sky Survey (SDSS; York et al. 2000), Radial Velocity Experiment (RAVE; Steinmetz et al. 2006), Apache Point Observatory

⋆ Based on observations collected with the Large Sky Area Multi-Object Fiber Spectroscopic Telescope (LAMOST) located at the Xinglong observatory, China.
⋆⋆ Full Tables A.3 and A.4 are only available at the CDS via anonymous ftp to cdsarc.u-strasbg.fr (130.79.128.5) or via http://cdsarc.u-strasbg.fr/viz-bin/qcat?J/A+A/594/A39

Galactic Evolution Experiment (APOGEE; Allende Prieto et al. 2008), *Gaia*-ESO (Gilmore et al. 2012), Large sky Area Multi-Object fiber Spectroscopic Telescope (LAMOST) Spectral Survey (Zhao et al. 2012), and many others provide vast databases of photometric and spectroscopic observations that aim at detailed investigations of the Galaxy and beyond and that also open the possibility for discoveries that are not predicted by the original scientific concept.

Apart from those systematic projects that aim to cover large portions of the sky, including different components of the Galaxy (bulge, thin and thick disk, open and globular clusters), there are also more specific observing projects that observe smaller sky areas and/or are conceived to give support to space missions. Among these, it is worth mentioning the ground-based, follow-up observations of *Kepler* asteroseismic targets coordinated by the *Kepler* Asteroseismic Science Consortium (KASC; see Uytterhoeven, et al. 2010) or the *Kepler* Community Follow-up Observing Program (CFOP), which associates individuals interested in providing ground-based observational support to the *Kepler* space mission[1]. Other large projects that aim to derive parameters for large samples of the *Kepler* sources are the SAGA (Casagrande et al. 2014, 2016) and the APOKASC (Pinsonneault et al. 2014) surveys. The former is based on Strömgren photometry, while the latter, which is still running, relies on intermediate-resolution infrared spectra taken in the framework of the APOGEE survey.

The LAMOST-*Kepler* project (hereafter the LK project) is part of the activities realized in the framework of the KASC. It aims at deriving the effective temperature ($T_{\rm eff}$), the surface gravity ($\log g$), the metallicity ([Fe/H]), the radial velocity (RV), and the projected rotational velocity ($v \sin i$) of tens of thousands of stars, which fall in the field of view of the *Kepler* space telescope (hereafter the *Kepler* field), as described in detail by De Cat et al. (2015; hereafter Paper I). The purpose of those measurements is multifarious. First, the atmospheric parameters yielded by the LK project complement and can serve as a test-bench for the content of the *Kepler* Input Catalog (KIC, Brown et al. 2011) and, as such, they provide firm bases for asteroseismic and evolutionary modeling of stars in the *Kepler* field. Second, our data enables us to flag interesting objects as it allows us to identify fast-rotating stars and those for which the variability in radial velocity exceeds ~20 km s^{-1}. Similarly, stars that show strong emission in their spectral lines or display other relevant spectral features can be identified and used for further research reaching beyond asteroseismic analysis. The analysis of the spectra obtained in the framework of the LK project is performed by three analysis teams with different methodologies. The American team uses the MKCLASS code to produce an MK spectral classification (Gray et al. 2016), the Asian team derives the atmospheric parameters and radial velocities by means of the LASP pipeline (Wu et al. 2014; Ren et al. 2016), the European team, whose results are presented in the present paper, adopt the code ROTFIT for deriving the atmospheric parameters, radial velocity, projected rotational velocity, and activity indicators.

As the selection of the targets and technical details of observations and reductions have been described in detail in Paper I, we focus in the present paper on the results we obtained with the code ROTFIT, developed by Frasca et al. (2003, 2006), and discussed in detail in Molenda-Żakowicz et al. (2013). This code has been adapted to the LAMOST data as described in Sect. 3. Here, we present the catalog containing the products of our analysis (the spectral type SpT, $T_{\rm eff}$, $\log g$, [Fe/H], RV, $v \sin i$, and the activity indicators $EW_{\rm H\alpha}$, EW_{8498}, EW_{8542}, and EW_{8662}) and discuss the precision and accuracy of the stellar parameters derived with ROTFIT. This is achieved by carrying out detailed comparisons between the results produced by that code and those available in the literature for the stars in common.

This paper is organized as follows. In Sect. 2 we briefly describe the observations. Sect. 3 presents the methods of analysis and discusses the accuracy of the data. This section includes a brief description of the ROTFIT pipeline, the procedure for the measure of the activity indicators, and a comparison of the RVs and atmospheric parameters derived in this work with values from the literature. The results from the activity indicators are presented in Sect. 4. We summarize the main findings of this work in Sect. 5.

2. Observations

Located at the Xinglong observatory (China), LAMOST is a unique astronomical instrument that combines a large aperture (3.6-4.9 m) with a wide field of view (circular with a diameter of 5°), which is covered with 4000 optical fibers connected to 16 multiobject optical spectrometers with 250 fibers each (Wang et al. 1996; Xing et al. 1998). For the LK project, we selected 14 LAMOST fields of view (FOVs) to cover the *Kepler* field. The data that are analyzed in this paper are those acquired with the LAMOST during the first round of observations. For a detailed description of these observations, we refer to Paper I. A total of 101 086 spectra for objects in the *Kepler* field were gathered during 38 nights from 30 May 2011 to 29 September 2014. The spectra were reduced and calibrated with the LAMOST pipeline as described by Luo et al. (2012, 2015). The integration times of individual exposures were set according to the typical magnitude of the selected subset of targets and to the weather conditions. These exposures range between 300 to 1800 s (see Table 2 of De Cat et al. 2015). In general, the observation of a plate, which denotes a unique configuration of the fibers, consists of a combination of several of such individual exposures of the same subset of targets. Therefore, the total integration times of the observed plates reaches values between 900 and 4930 s.

Since the exposure time is the same for all stars observed within a plate, the signal-to-noise ratio (S/N) of the acquired spectra varies significantly from target to target, which is mainly a reflection of their magnitude distribution. Because the number of available LAMOST spectra is huge, we decided to semiautomate the process of selection of high- and low-quality spectra using the information yielded by the LAMOST pipeline, namely, the values of S/N at the effective wavelengths of the Sloan DSS filters *ugriz* (Fukugita et al. 1996; Tucker et al. 2006) and the spectral type given either in the Harvard system or in a free, descriptive system of classification used in the LAMOST pipeline (e.g., *carbon* or *flat*). For targets classified by the LAMOST pipeline as A, F, G, or K-type, we rejected spectra with $S/N < 10$ in the *r* filter. Spectra of targets classified to the other types were checked by eye to find and reject those that contain only noise. In Fig. 1, we show histograms of S/N at the *ugriz* filters for the LAMOST spectra for which we derived the atmospheric parameters. In Table 1, we give an overview of the analyzed LAMOST spectra. In total, the atmospheric parameters were derived from 61,753 LAMOST spectra, which correspond to 51 385 unique targets, including 30 213 stars that were observed by *Kepler*. For 8832 objects, more than one LAMOST spectrum was analyzed.

[1] https://cfop.ipac.caltech.edu

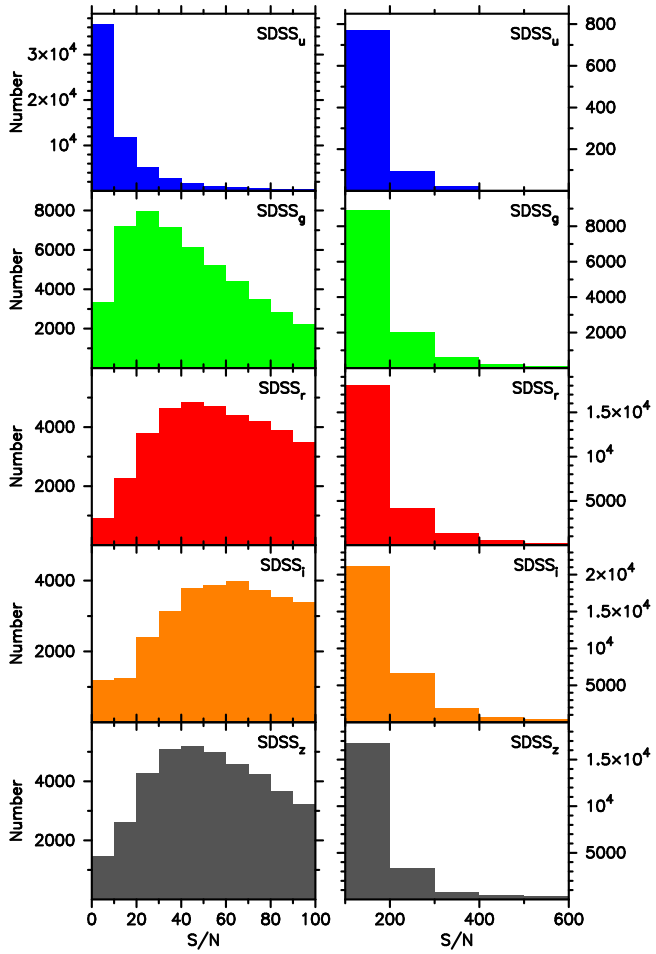

Fig. 1. Histograms of the S/N of the spectra from which we derived the atmospheric parameters with the ROTFIT code measured at the effective wavelengths of the Sloan DSS filters *ugriz*. The *left and right* panels show the S/N range [0, 100] with bin size 10 and the S/N range [100, 600] with bin size 100, respectively.

Table 1. Statistical overview of the analyzed LAMOST spectra that have been obtained before the end of the 2014 observation season for the *Kepler* FOV.

Field	RA(2000)	Dec(2000)	Date	#	Spectra	KO
LK01	19:03:39.26	+39:54:39.2	110 530	1	939	411
			110 608	2	711	370
			140 602	2	3386	1846
LK02[a]	19:36:37.98	+44:41:41.8	120 604	1	382	247
			140 913	2	5439	3469
LK03[b]	19:24:09.92	+39:12:42.0	120 615	3	4614	3381
LK04[c]	19:37:08.86	+40:12:49.6	120 617	3	4206	2769
LK05	19:49:18.14	+41:34:56.8	131 005	2	3271	2247
			140 522	1	1170	865
LK06	19:40:45.38	+48:30:45.1	130 522	1	1774	1317
			130 914	1	2234	1530
LK07	19:21:02.82	+42:41:13.1	130 519	1	1778	1340
			130 926	1	2324	1772
LK08[d]	19:59:20.42	+45:46:21.1	130 925	2	4330	1759
			131 002	1	100	31
			131 017	1	1674	660
			131 025	1	2147	821
LK09	19:08:08.34	+44:02:10.9	131 004	1	2462	1702
LK10	19:23:14.83	+47:11:44.8	140 520	2	2041	1395
LK11	19:06:51.50	+48:55:31.8	140 918	1	2589	1649
LK12	18:50:31.04	+42:54:43.7	131 007	1	2111	1170
LK13	18:51:11.99	+46:44:17.5	140 502	1	1921	1075
			140 529	2	3410	1841
LK14	19:23:23.79	+50:16:16.6	140 917	1	2588	1397
			140 927	1	1814	974
			140 929	1	2338	1158
Total					61 753	37 196
Unique					51 385	30 213
1×					42 553	24 303
2×					7569	5007
3×					1079	784
4×					117	81
+5×					67	38

Notes. The top lines give the specifications of the LK fields that have been observed. For each LK field, we give the right ascension (RA(2000)) and declination (DE(2000)) of the centrum, date of observation (YYMMDD; Date), number of plates that were used to observe the LK field (#), number of spectra for which we derived the atmospheric parameters with the ROTFIT code (Spectra), and number of spectra that correspond to a target that was observed by the *Kepler* mission (KO). The bottom lines give the summary of the observations of all LK fields together. We give the total number of spectra for which we derived the atmospheric parameters with the ROTFIT code (Total), number of different objects that were analyzed (Unique), and number of targets for which we obtained one (1×), two (2×), three (3×), four (4×), and at least five (+5×) sets of atmospheric parameters. [(a)] Includes the cluster NGC 6811. [(b)] Includes the cluster NGC 6791. [(c)] Includes the cluster NGC 6819. [(d)] Includes the cluster NGC 6866.

3. Data analysis

3.1. Radial velocity

The radial velocity was measured by means of the cross-correlation between the target spectrum and a template chosen among a list of 20 spectra of stars with different spectral types (Table 2) taken from the Indo US library (Valdes et al. 2004). We chose stars with $v \sin i$ as low as possible to minimize the enlargement of the cross-correlation function (CCF). However, given the low resolution of the LAMOST spectra ($R \simeq 1800$ with the slit width at 2/3 of the fiber size) and the coarse grid of spectral points, where the spacing corresponds to about 70 km s^{-1}, only stars that are rotating faster than about 120 km s^{-1} can have an appreciable effect on the CCF (see Sect. 3.2).

The Indo-US spectra are suitable RV templates, since they are in the laboratory frame, i.e., the barycentric correction was already applied and the RV of the star subtracted. We only had to handle the continuum normalization.

Each LAMOST spectrum was split into eight spectral segments centered at about 4000, 4500, 5000, 5500, 6200, 6700, 7900, and 8700 Å, and, for each segment, the CCF with each template listed in Table 2 was computed. We therefore developed an ad hoc code in the IDL[2] environment. The best template was selected based on the height of the peak. To evaluate the centroid and full width at half maximum (FWHM) of the CCF peak, we fitted it with a Gaussian. For each spectral segment, the RV error, σ_i, was estimated by the fitting procedure curvefit

[2] IDL (Interactive Data Language) is a registered trademark of Exelis Visual Information Solutions.

Table 2. Templates adopted for the cross-correlation.

Name	Sp. type	$T_{\rm eff}$[a] (K)	$v \sin i$ (km s^{-1})
HD 47839	O7 Ve	40175	67[b]
HD 180 163	B2 .5IV	18946	10[c]
HD 17081	B7 IV	12678	25[c]
HD 123 299	A0 III	10307	25[d]
HD 34578	A5 II	8570	14[d]
HD 25291	F0 II	7761	13[e]
HD 33608	F5 V	6428	16.0[f]
HD 88986	G0 V	5787	1.0[f]
HD 115 617	G5 V	5598	1.1[g]
HD 145 675	K0 V	5292	0.6[h]
HD 32147	K3 V	4617	0.8[i]
HD 88230	K8 V	3947	3.1[h]
G 227-46	M3 V	3481	<2.8[l]
HD 204 867	G0 Ib	5705	6.3[m]
HD 107 950	G6 III	5176	6.6[n]
HD 417	K0 III	4858	1.7[n]
HD 29139	K5 III	3863	2.0[n]
HD 168 720	M0 III	3789	...
HD 123 657	M4 III	3235	...
HD 126 327	M8 III	3088	...

References. [(a)] Wu et al. (2011); [(b)] Howarth (1997); [(c)] Abt et al. (2002); [(d)] Royer et al. (2002); [(e)] Abt & Morrel (1995); [(f)] Nordström et al. (2004); [(g)] Queloz et al. (1998); [(h)] Fekel (1997); [(i)] Saar & Osten (1997); [(l)] Delfosse et al. (1998); [(m)] Gray & Toner (1987); [(n)] de Medeiros & Mayor (1999).

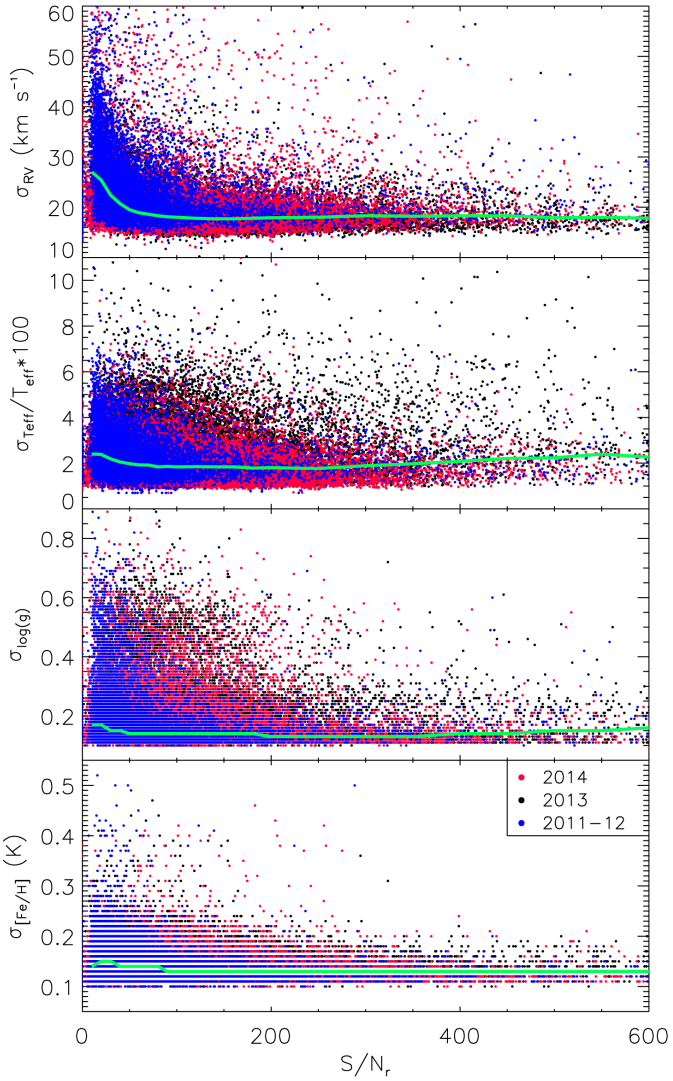

Fig. 2. Scatter plots with the errors of RV, $T_{\rm eff}$, log g, and [Fe/H] (*from top to bottom*) as a function of the S/N in the r band. The following color coding is used: blue for 2011–2012, black for 2013, and red for 2014. The full green line, in each box, is the median value as a function of S/N.

(Bevington 1969), taking the CCF noise into account, which was evaluated far from the peak ($|\Delta RV| > 4000$ km s^{-1}). The final RV for each star was obtained as the weighted mean of the values of all the analyzed spectral segments, using as weights $w_i = 1/\sigma_i^2$, and applying a sigma clipping algorithm to reject outliers. The standard error of the weighted mean was adopted as the estimate of the RV uncertainty, σ_{RV}. The resulting RV and σ_{RV} values are given in columns 15 and 16 of Table A.3.

The RV errors are typically in the range 10–30 km s^{-1} with an average value of about 20 km s^{-1}. These errors are in line with what is expected on the basis of the LAMOST resolution and data sampling. In particular, less than 0.03% of the stars have an error $\sigma_{RV} \leq 10$ km s^{-1}, while $10 \leq \sigma_{RV} < 20$ km s^{-1} for 66% of the full sample, $20 \leq \sigma_{RV} < 30$ km s^{-1} for 29% , $30 \leq \sigma_{RV} < 40$ km s^{-1} for about 3.5%, and $\sigma_{RV} \geq 40$ km s^{-1} for about 1.5% of the sample. The behavior of these errors as a function of SNR$_r$ is shown in Fig. 2. The median value ranges from about 18 km s^{-1} to 27 km s^{-1}as a function of S/N.

An empirical determination of the measurement uncertainty, however, can be performed by comparing repeated measurements of RV for the same star in different spectra (e.g., Yanny et al. 2009; Jackson et al. 2015). The distribution of the RV differences is plotted in Fig. 3a. This distribution shows broad tails and it is best fitted by a double-exponential (Laplace) function (see, e.g., Norton 1984) rather than by a normal distribution (Gaussian). The standard deviation of the Laplace fit is $\sqrt{2}b = 16.6$ km s^{-1}, where b is the dispersion parameter of the Laplace function. Considering that this distribution is for RV differences of couples of measures, we must divide by $\sqrt{2}$ to obtain an estimate of the average error on each individual measure (e.g., Jackson et al. 2015), which is $b = 11.7$ km s^{-1}. This may suggest a slightly better RV precision than that indicated by the individual RV errors reported in Table A.3 and plotted in Fig. 2.

For 104 of the stars that we analyzed, we found RV values in the literature that come from high- or mid-resolution spectra. We discarded the stars known to be spectroscopic binaries (SB) and those with large pulsation amplitudes, for example, Mira-type variables, even if their RV variations are small compared to the typical LAMOST RV errors. To validate the RV determinations and to evaluate their external accuracy, we compared our measurements with those from the literature. The results are shown in Fig. 4. The RV values and errors are also reported in Table A.1 together with those from the literature for these stars. For most of these objects we have only one LAMOST spectrum, but for some of them we have from two to four different spectra with a total of 133 RV values. As it appears in Fig. 4, our values of RV are consistent with the literature values within 3σ. There is only one star for which we found at least one discrepant RV value; this star is indicated with a filled circle enclosed in an open square in Fig. 4. We considered an RV value as discrepant when $|RV_{\rm LAM} - RV_{\rm Lit}| \geq 3\sqrt{(\sigma_{\rm RV}^{\rm LAM})^2 + (\sigma_{\rm RV}^{\rm Lit})^2}$, i.e., when the

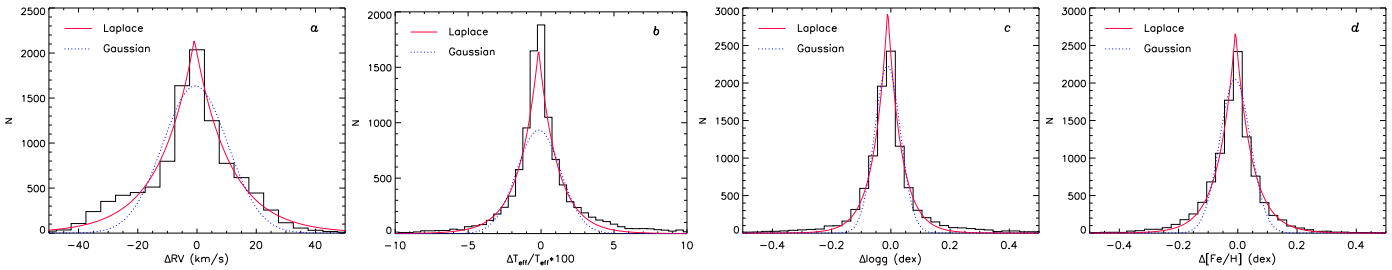

Fig. 3. Distributions of the differences of RV, $T_{\rm eff}$, $\log g$, and [Fe/H] for the stars with repeated observations (histograms). In each box, the full line is the double-exponential (Laplace) fit, while the dotted line is the Gaussian fit.

RV difference is larger than three times the quadratic sum of the errors. This object is KIC 7599132 (=HD 180757), which has been classified as a rotationally variable star by McNamara et al. (2012). We inserted this star in our ongoing campaign at the Catania Astrophysical Observatory aimed at a spectroscopic monitoring of newly discovered binary systems. As a very preliminary result, we can confirm its RV variations. The full results of this spectroscopic monitoring will be presented in a forthcoming paper.

This example shows that the LAMOST RVs are accurate enough to detect pulsating stars or single-lined spectroscopic binary systems (SB1) with a large variation amplitude (ΔRV $>$ 50 km s^{-1} when $\sigma_{\rm RV} \leq 20$ km s^{-1}) among the stars with multiple observations. To this purpose, for stars with multiple observations, we calculated the reduced χ^2 and probability $P(\chi^2)$ that the RV variations have a random occurrence (e.g., Press et al. 1992). The values of $P(\chi^2)$ are quoted in column 19 of Table A.3.

On average, the offset between the LAMOST and literature RVs is only +5 km s^{-1} and the rms scatter of our data around the bisector is $\simeq$14 km s^{-1}, which confirms the reliability of our RV measurements and their errors. In any case, if we take into account that some of these stars, especially those with only one LAMOST RV value, could indeed be undetected SBs, the dispersion of 14 km s^{-1} can be considered an upper limit for the accuracy of our RV determinations.

The procedure for the measurement of RV was run inside the code for the determination of the atmospheric parameters (see Sect. 3.2), since the RV was needed to align in wavelength the reference spectra with the observed one.

3.2. Projected rotation velocity and atmospheric parameters

We estimated the projected rotation velocity, $v \sin i$, and the atmospheric parameters (APs), $T_{\rm eff}$, $\log g$, and [Fe/H] with a version of the ROTFIT code (e.g., Frasca et al. 2003, 2006), which we adapted to the LAMOST spectra. We adopted, as templates, the low-resolution spectra of the Indo-US Library of Coudé Feed Stellar Spectra (Valdes et al. 2004) whose parameters were recently revised by Wu et al. (2011). This library has the advantage of containing a large number of spectra of different stars, which sufficiently cover the space of the atmospheric parameters, even if the density of templates is not uniform and is rather low in the very metal poor regime. Although the small number of metal-poor templates is a limit for the determination of the APs, the use of spectra of real stars is beneficial for spectral subtraction, as the synthetic spectra are more prone to problems in the cores of Hα and Ca II-IRT lines (see, e.g., Linsky et al. 1979; Montes et al. 1995).

The resolution of $\approx$1 Å and the sampling of 0.44 Å pixel^{-1} are both higher than the LAMOST resolution and sampling, and allow us to properly degrade the Indo-US spectra to match the

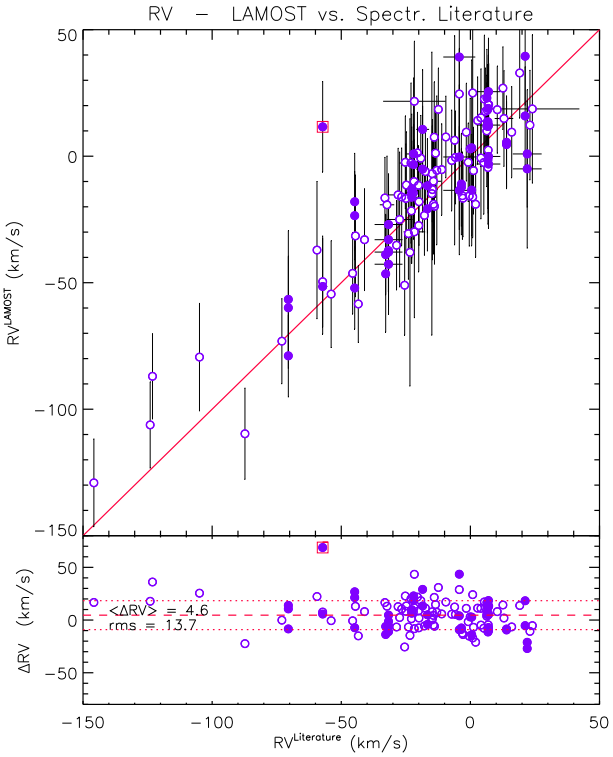

Fig. 4. *Top panel*: comparison between the RV measured on LAMOST spectra (Table A.1) with literature values based mainly on high-resolution spectra (open circles). Filled circles refer to stars with multiple LAMOST observations. The continuous line is the one-to-one relationship. The differences, shown in the *bottom panel*, show a mean value of $\simeq$+5 km s^{-1} (dashed line) and a standard deviation of about 14 km s^{-1} (dotted lines). Discrepant values are indicated with filled circles enclosed in squares in both panels.

LAMOST resolution and to resample them on the same wavelength scale as the LAMOST spectra. Furthermore, the wavelength range covered by these spectra (from 3465 to 9470 Å) is larger than the wavelength range of the LAMOST spectra (from 3700 to 9000 Å), which allows us to exploit all the information contained in the LAMOST spectra for our analysis. We discarded those stars for which some parts of the spectrum were missing from the full library and kept 1150 templates.

In the first step, the reference spectra were aligned onto the target spectrum as a result of the radial velocity measured as described in Sect. 3.1. In the second step, each template was broadened by the convolution with a rotational profile of increasing $v \sin i$ (in steps of 5 km s^{-1}) until a minimum of the residuals was reached. This can provide us with an estimate of $v \sin i$. However, given the low resolution of the LAMOST spectra, $R \simeq 1800$,

which corresponds to about 170 km s^{-1}, and the spectra sampling of about 70 km s^{-1}, this parameter is badly defined. We were only able to use it to unambiguously identify the very fast rotators in our sample. We ran Monte Carlo simulations with LAMOST spectra of a few stars, known to be slow rotators from the literature, with the aim of estimating the minimum $v \sin i$ that can be measured with our procedure. These spectra were artificially broadened by convolution with a rotation profile of increasing $v \sin i$ (in steps of 30 km s^{-1}) and a random noise was added, similar to Frasca et al. (2015). We found that the rotational broadening is unresolved up to 90 km s^{-1} and we start to resolve it when $v \sin i \geq 120$ km s^{-1}. We therefore can only trust $v \sin i$ values above 120 km s^{-1}. For stars with a resulting $v \sin i$ value below 120 km s^{-1}, the calculated value was replaced by <120 km s^{-1} and flagged as an upper limit in Table A.3.

As for the RV, we split the spectrum into eight spectral segments that were analyzed independently. The templates were then sorted in a decreasing order of the residuals, giving the highest score to the best-fitting template. The spectral type of the template with the highest total score, summing up the results of the individual spectral regions, was assigned to the target star. An example of the fit of an early A-type star, in five spectral segments, is shown in Fig. A.1. Two other examples are shown in Figs. A.2 and A.3 for an F5 V and a K0 III star, respectively.

For each segment we derived values of $T_{\rm eff}$, $\log g$, and [Fe/H] and their standard errors, which were based on the parameters of the ten best matching templates. The final APs were obtained as the weighted mean of those of the individual segments and are reported in Cols. 9, 11, and 13 of Table A.3, respectively. We adopted as uncertainties for $T_{\rm eff}$, $\log g$, and [Fe/H] the standard errors of the weighted means to which the average uncertainties of the APs of the templates (±50 K, ±0.1 dex, ±0.1 dex, respectively) were added in quadrature. Scatter plots of APs errors as a function of the S/N in the r band are shown in Fig. 2.

We also considered the stars with two or more spectra for the evaluation of the AP uncertainties, as we did for the RV. The distributions of $T_{\rm eff}$, $\log g$, and [Fe/H] differences are indicated with the histograms in Figs. 3b, c, and d, respectively. All these distributions are best fitted by a double-exponential function whose dispersion parameter b indicates an average uncertainty of about 66 K or 1.3% for $T_{\rm eff}$, 0.046 dex for $\log g$, and 0.055 dex for [Fe/H]. These values are all significantly smaller than the average errors (full lines in Fig. 2), which are likely slightly overestimated.

Both these evaluations of uncertainties are internal to the procedure and do not reveal the accuracy of the APs derived with ROTFIT and the templates' grid of choice. To this aim we compared the parameters that were derived in the present work with those available for some stars from the literature. The literature values were mainly derived from high-resolution optical spectra and, in some cases, with asteroseismic techniques. The APs derived from LAMOST spectra, together with those found in the literature (468 stars with $T_{\rm eff}$ data, of which 352 and 350 also have $\log g$ and [Fe/H] values, respectively), are listed in Table A.2. The results of the comparison are shown in Fig. 5.

We note the very good agreement between the $T_{\rm eff}$ values with an average offset of only +30 K and an rms of 150 K in the temperature range 3000–7000 K (FGKM spectral types). As the errors of $T_{\rm eff}$ determinations usually grow with the temperature, we preferred to plot the logarithm of temperature in Fig. 5, whose dispersion, $\sigma_{\log(T_{\rm eff})} = 0.4343\sigma_{\ln(T_{\rm eff})} \simeq 0.4343\sigma_{T_{\rm eff}}/T_{\rm eff}$, is a measure of the relative accuracy of temperature. This turns out to be $\sigma_{T_{\rm eff}}/T_{\rm eff} \simeq 3.5\%$ with no significant systematic offset with respect to the literature values.

The $\log g$ values display instead a larger scatter, which amounts to about 0.30 dex and a tendency for our values to cluster around 2.5 (the typical $\log g$ of the K stars in the red giant branch) and 4–4.5 (main-sequence stars). This is likely the result of the different density of templates as a function of $\log g$ that, at any given $T_{\rm eff}$, are more frequent at $\log g \simeq 4.5$ and $\log g \simeq 2.5$, giving rise to a possible bias toward MS or red-giant gravities in the average $\log g$. We note that our analysis code derives a correct $\log g$ for several stars with literature values of $\log g$ that are intermediate between MS and giants or lower than 2.5. This comparison shows that the $\log g$ values are not very accurate, but we are still able to distinguish between luminosity classes I, III, and V, which, together with an accurate $T_{\rm eff}$ determination unaffected by interstellar extinction, was one of the main aims of this analysis. Indeed, this is the requirement for performing a trustworthy spectral subtraction and flux calibration of the chromospheric EWs (see Sect. 3.4) because the surface continuum flux depends mainly on $T_{\rm eff}$ and exhibits only a second-order dependence on $\log g$ that is properly considered with our gravity estimates (see Appendix C).

The [Fe/H] values are only in good agreement with the literature values around the solar metallicity, i.e., between −0.3 and +0.2. We tend to overestimate [Fe/H] when it is lower than −0.3 and to underestimate it for values higher than +0.2. Although the data scatter could be due to the low resolution of the spectra, the systematic trend is likely an effect of the relative scarcity of metal poor and super metal rich stars among our templates. Interestingly, the very low value of metallicity for KIC 9206432 ([Fe/H] = −2.23) has been correctly found by ROTFIT in the LAMOST spectrum, which indicates a negligible contamination by metal richer templates. A linear fit to the values with $[{\rm Fe/H}]_{\rm Lit} > -1.5$ (dashed line in Fig. 5c) gives a slope of $m = 0.428 \pm 0.029$.

A large and very recent data set of APs for red giants in the *Kepler* field is given in the APOKASC catalog (Pinsonneault et al. 2014). They analyzed APOGEE near-IR spectra, complemented with asteroseismic surface gravities. We found 787 stars in common. The comparison of the APs for these stars is shown in Fig. 6. Even if the ranges of $T_{\rm eff}$ and $\log g$ values are smaller than those of Fig. 5, these plots show the same general trends as in Fig. 5. In particular, the agreement of $T_{\rm eff}$ is rather good with an rms dispersion of 127 K and only two outliers that we denoted with open squares.

The $\log g$ values display a systematic deviation from the one-to-one relation, which is similar to that shown by the giant stars in Fig. 5 with the LAMOST gravities clustered around the average value of red giants (∼2.5). This behavior is clearly shown by the differences plotted in the lower box. The outliers of the $T_{\rm eff}$ plot show also discrepant $\log g$ values; these values are indicated with red dots enclosed in open squares in Fig. 6b and the properties of these objects are described in Appendix B.

The plot of [Fe/H] comparison is very similar to that of Fig. 5. In this case the systematic trend of the LAMOST versus APOKASC metallicity is even more evident and best fitted with a linear relation in the range $[{\rm Fe/H}]_{\rm APOKASC} > -1.5$, which roughly corresponds to $[{\rm Fe/H}]_{\rm LAMOST} > -1.0$. We find a slope $m = 0.464 \pm 0.017$, which is close to that of the fit of Fig. 5. We thus propose a correction relation for the LAMOST metallicity, based on this linear fit, which can be expressed as

$$[{\rm Fe/H}]_{\rm corr} = 2.16 \cdot [{\rm Fe/H}] + 0.17, \quad (1)$$

applicable in the range

$$[{\rm Fe/H}] > -1.0.$$

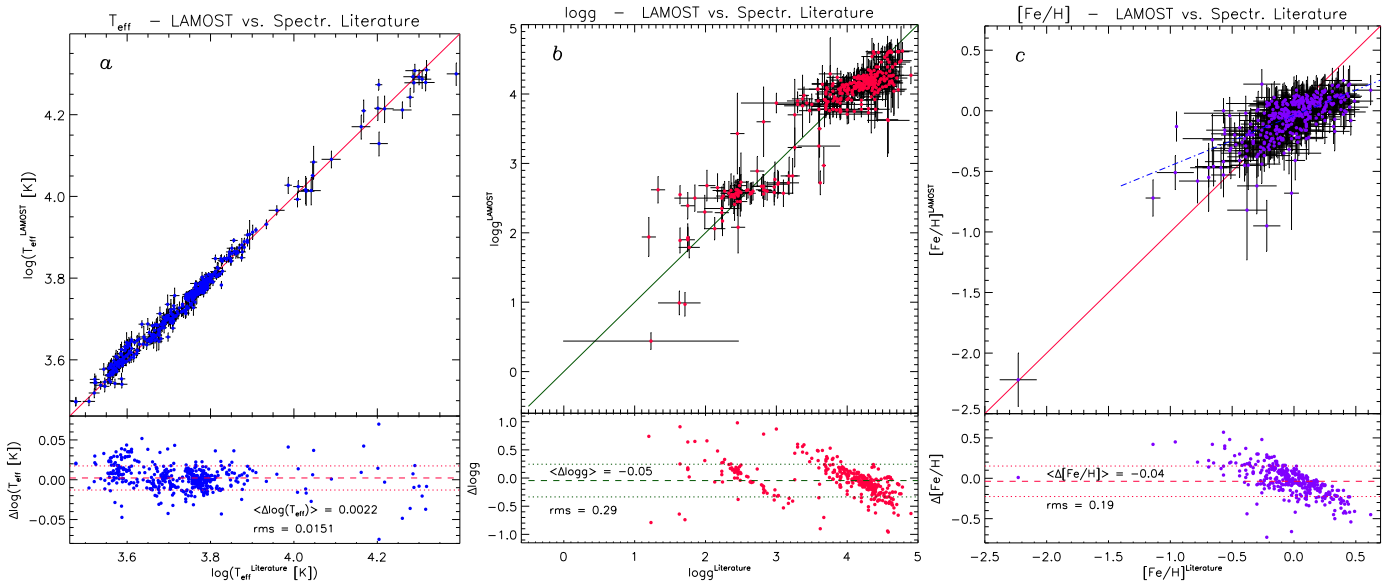

Fig. 5. Comparison between the atmospheric parameters measured on LAMOST spectra with literature values. The continuous lines in *the top panels* represent one-to-one relationships, as in Fig. 4. The dash-dotted line in the [Fe/H] plot (panel **c**)) is a linear fit to the data with $[Fe/H]_{Lit} > -1.5$. The differences are shown in the bottom panels along with their average values and standard deviations.

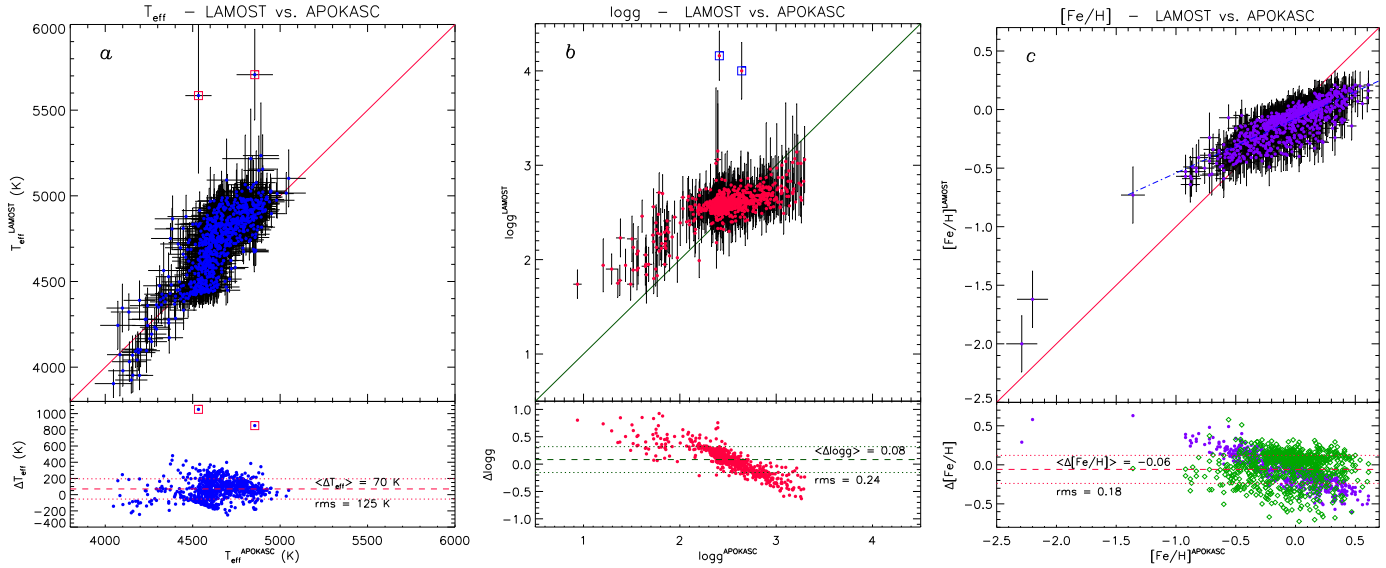

Fig. 6. Comparison between the atmospheric parameters of red giants in the APOKASC catalog and in our database of LAMOST spectra. The meaning of symbols and lines is the same as in Fig. 5. The open diamonds in the *bottom box* of panel **c)** refer to [Fe/H] values corrected according to Eq. (1).

The LAMOST values of [Fe/H] corrected with the above equation are plotted in the bottom panel of Fig. 6 as green open diamonds. As shown in the figure, the trend has disappeared at the cost of a greater dispersion of the data. However, we prefer to report, in Table A.3, the [Fe/H] values as derived by our code without applying any correction to them, but these raw values should be corrected with Eq. (1) (or with purposely developed relations in their proper range of validity) before they are used.

Another large set of atmospheric parameters for stars in the *Kepler* field is represented by the SAGA catalog (Casagrande et al. 2014), which is based on asteroseismic data and Strömgren photometry. Currently, this catalog contains parameters for about 1000 objects, 287 of which have been analyzed in the present paper. The results of the comparison of LAMOST and SAGA parameters are shown in Fig. 7, where symbols and lines have the same meaning as in Figs. 5 and 6. The comparison with SAGA data displays behaviors similar to those already found with the other data sets. Some outliers were also detected and indicated with open squares in Fig. 7. These outliers are briefly discussed in Appendix B.

Similar to what we did for [Fe/H], we made an attempt to find a correction relation for $\log g$. For this purpose we considered all the stars with $\log g$ values in the literature (Fig. 5b) from the APOKASC (Fig. 6b) and the SAGA (Fig. 7b) catalogs. These data are shown together, using different symbols, in Fig. 8. As the $\log g$ values are basically grouped into two separate regions, we performed two different linear fits for $\log g < 3.3$

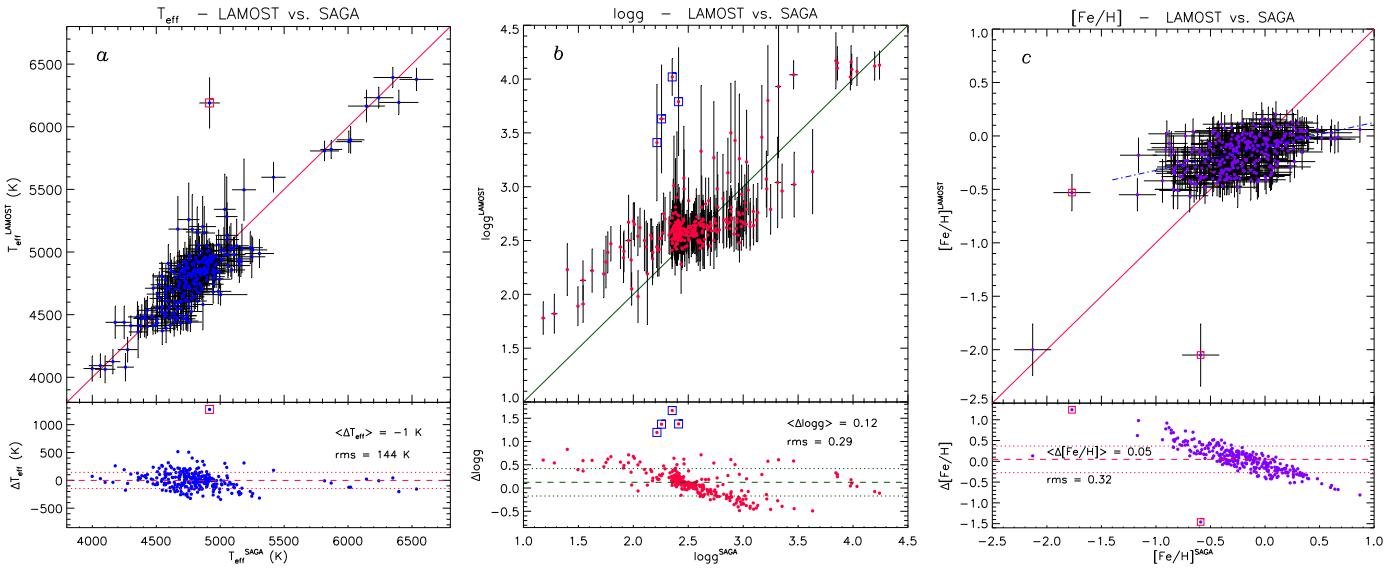

Fig. 7. Comparison between the atmospheric parameters in the SAGA catalog and in our database of LAMOST spectra. The meaning of symbols and lines is the same as in Fig. 5.

and $\log g \geq 3.3$, which are shown in Fig. 8 by the dash-dotted and dashed lines, respectively, and are given by the following equations:

$$\log g_{\rm corr} = 2.01 \cdot \log g - 2.70 \qquad (\log g < 3.3) \qquad (2)$$
$$\log g_{\rm corr} = 1.88 \cdot \log g - 3.55 \qquad (\log g \geq 3.3).$$

This correction removes much of the nearly linear trends that appear in the bottom panel of Fig. 8, although the scatter is enhanced. As with [Fe/H], we report only the original values, without any correction, in Table A.3.

3.3. Statistical properties of the LAMOST-Kepler sample

Figure 9 shows a comparison of the metallicity distributions of the LAMOST-*Kepler* targets derived in the present work (where [Fe/H] has been corrected according to Eq. (1)) with those from the KIC catalog and from the work of Huber et al. (2014). For a meaningful comparison, we selected all the stars in common between these three catalogs (30 104 stars). The different distributions of LAMOST and KIC metallicities is apparent. The mean and median for the LAMOST data are −0.05 and +0.02 dex, respectively, while for the KIC data they are −0.17 and −0.13 dex, respectively. This result is in close agreement with the finding of Dong et al. (2014), which strengthens the validity of the correction expressed by Eq. (1), at least in a statistical sense. The Huber et al. metallicities are distributed in a very similar way to that of the KIC catalog (mean = −0.19 dex; median = −0.16 dex). This is not surprising because the majority of these values are not spectroscopic and are mostly derived from the KIC photometry. Indeed, if we only consider the spectroscopic data in Huber et al. (2014), we find a mean of −0.02 dex and a median of −0.01 dex, which are much closer to those of the LAMOST data.

The RV distribution for the full sample of LAMOST spectra is shown in Fig. 10, in which we also overplot the RV distributions for the subsamples in three different metallicity ranges. The distribution is far from symmetric and displays a tail toward negative radial velocities. The asymmetry of the distribution is clearly enhanced with the decrease of metallicity, as expected from the higher percentage of high-velocity stars among the metal poor stars.

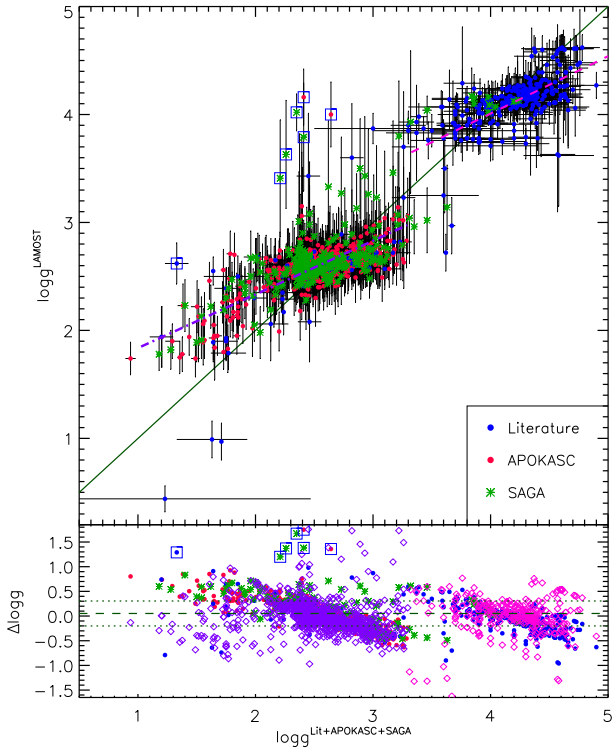

Fig. 8. Comparison between our $\log g$ values and those from the literature (blue dots), the APOKASC (red dots), and the SAGA (green asterisks) catalogs. Linear fits to the data with $\log g < 3.3$ and $\log g \geq 3.3$ are shown with the dash-dotted and dashed lines, respectively. The open diamonds in the *bottom panel* refer to values corrected according to Eq. (2).

As a further test on our results, we built the RV distribution obtained with the SEGUE data (Yanny et al. 2009) in the *Kepler* field. We selected stars with coordinates in the range 275° ≤ RA ≤ 305° and 35.5° ≤ Dec ≤ 52.5°. Because of the different selection criteria (mainly the limiting magnitude) for the *Kepler*-LAMOST and SEGUE surveys, only 13 stars are in common in the two samples. Nevertheless, the SEGUE sample

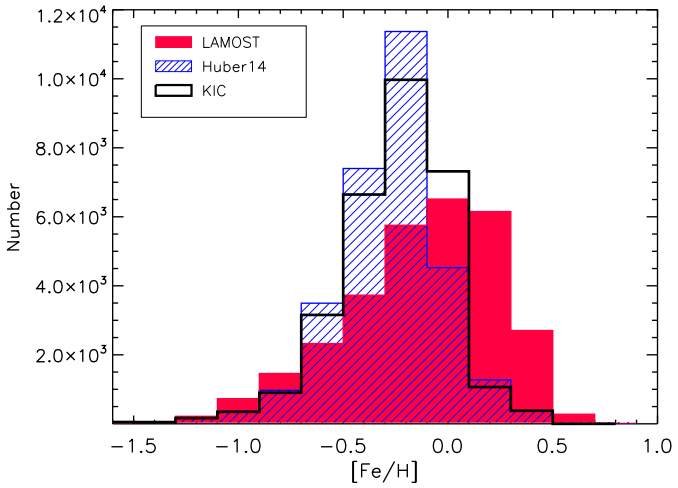

Fig. 9. [Fe/H] distribution (red filled histogram) for the LAMOST-*Kepler* subsample of stars in common with the Huber et al. (2014) catalog (blue hatched histogram). The metallicities from the KIC catalog are shown with the empty histogram.

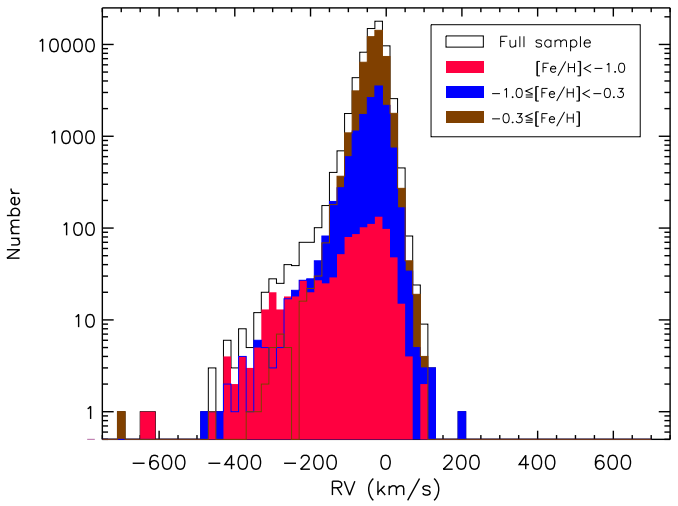

Fig. 10. RV distribution for the full sample of spectra (empty histogram) and for the subsamples in specific metallicity ranges, as indicated in the legend. A bin size of 20 km s^{-1} was used.

is composed of 3039 stars, which are spatially distributed as in Fig. 11a. Therefore it is statistically significant. As seen in Fig. 11b, its RV distribution shows a shape that is very similar to that of LAMOST RVs. These data also display the larger contribution of stars with negative velocity at low metallicities.

3.4. Activity indicators and spectral peculiarities

Despite the rather low resolution, which prevents a detailed study of individual spectral lines, the LAMOST spectra are also very helpful to identify objects with spectral peculiarities such as emission lines ascribable, for example, to magnetic activity for late-type stars or to the circumstellar environment and winds in hot stars.

The most sensitive diagnostics of chromospheres in the range covered by the LAMOST spectra are the Ca II H and K lines that lie, however, in a spectral region where the instrument efficiency is very low, compared to the red wavelengths. Moreover, the flux emitted by cool stars at the Ca II H and K wavelengths is very low

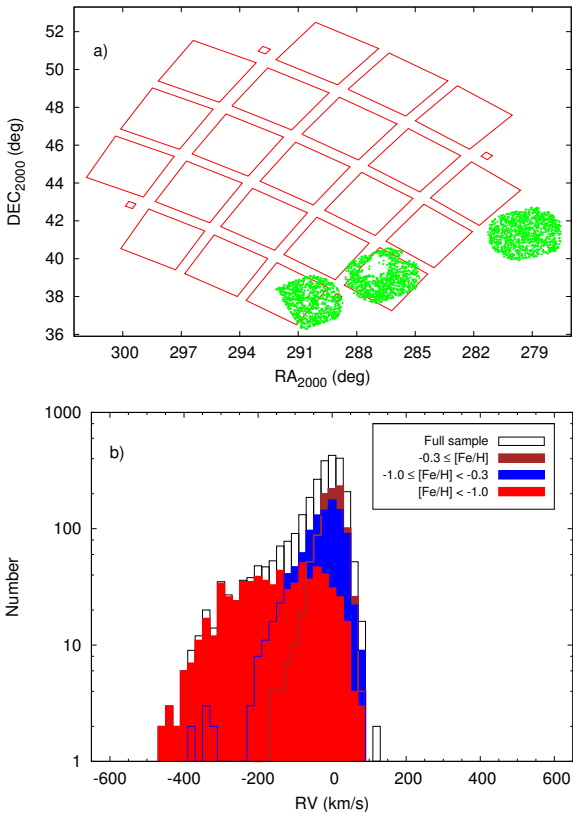

Fig. 11. *Upper panel*: spatial distribution of the SEGUE targets (dots) in the *Kepler* field. *Lower panel*: RV distribution for the SEGUE targets. A bin size of 20 km s^{-1} was used.

and, with the exception of the brightest targets, is dominated by the noise in the LAMOST spectra.

We have therefore used the Balmer Hα line to identify late-type or early-type objects with emission, which can be produced by various physical mechanisms. We subtracted the Indo-US template that best matches the final APs from each LAMOST spectrum. This template has been aligned to the target RV and resampled on its spectral points. The residual Hα emission, $EW^{\rm res}_{\rm H\alpha}$, was integrated over a wavelength interval of 35 Å around the line center (see Fig. 12, upper panel). The stars with a residual Hα equivalent width $EW^{\rm res}_{\rm H\alpha} \geq 1$ Å were selected as emission-line candidates. A visual inspection of their spectra allowed us to reject several false positives, which are the result of (i) a mismatch in the line wings between target and template; (ii) a spurious emission inside the Hα integration range, which derives from a residual cosmic ray spike; and (iii) problems occurring in spectra with a very low signal. This selection criterion can be too strict for some stars, such as K and M dwarfs, with a filled-in profile or an intrinsically narrow Hα emission of moderate intensity that can be smeared by the low resolution to a signature with an $EW^{\rm res}_{\rm H\alpha} < 1$ Å. For this reason we scrutinized all the spectra for which we found a $T_{\rm eff} < 5000$ K and a $\log g > 3.0$ integrating the residual Hα profile over a smaller range (16 Å) and adopting 0.3 Å as the minimum $EW^{\rm res}_{\rm H\alpha}$ value for keeping a star as a candidate. This allowed us to select, after a visual inspection of the results, additional stars that are likely to be active. As an example, we show in Fig. 13 the spectrum of KIC 4929016, which we classified as a K7V star ($T_{\rm eff} = 4035$ K). This star displays a weak Hα emission feature with an equivalent width of about 0.90 Å. This star has an RV (Table A.1) derived from the APOGEE survey of M dwarfs (Deshpande et al. 2013) and

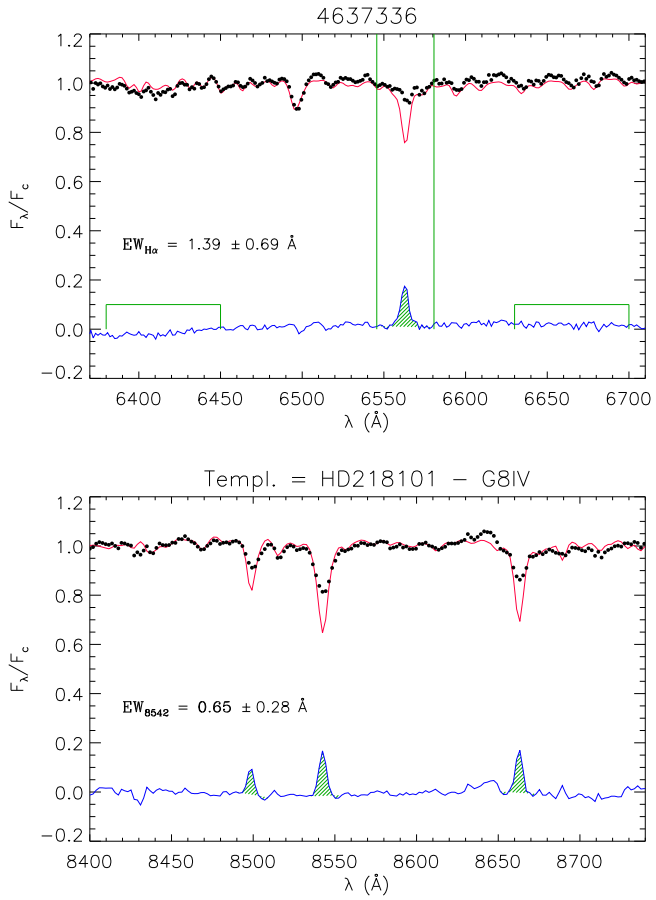

Fig. 12. *Upper panel*: LAMOST spectrum of KIC 4637336 (black dotted line), a late G-type star with the Hα totally filled in by emission. The inactive template is overplotted with a thin red line. The difference between target and template spectrum, plotted in the bottom of the panel (blue line), shows only a residual Hα emission (hatched area). The integration range for the residual equivalent width, $EW^{\rm res}_{\rm H\alpha}$ is indicated by the two vertical lines and the two regions used for the evaluation of the continuum setting error are also denoted. *Lower panel*: the spectral region around the Ca II infrared triplet (IRT) is shown with the same line styles as for Hα. The residual chromospheric emission in the cores of the Ca II IRT lines is outlined by the hatched areas.

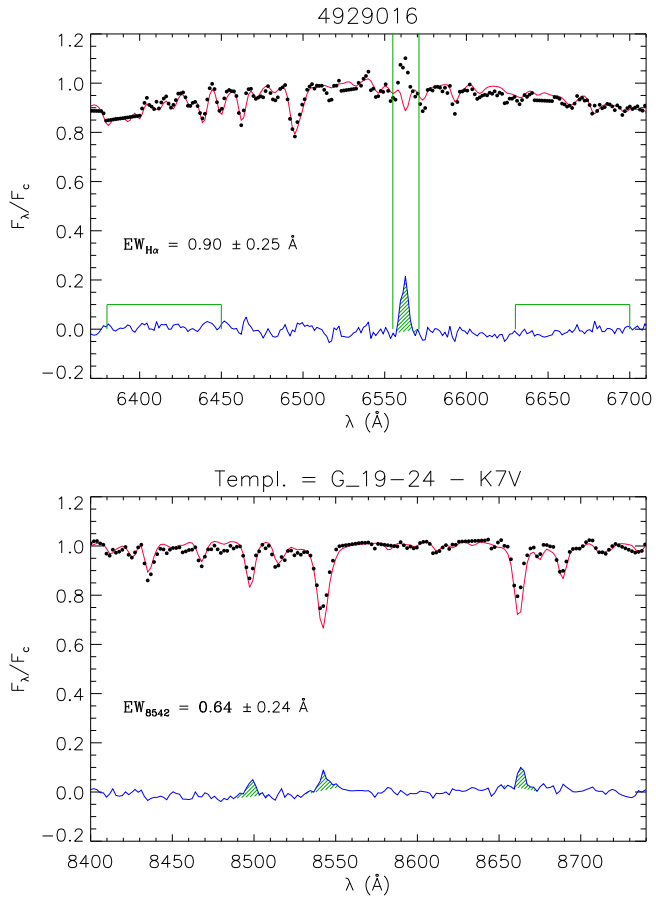

Fig. 13. Hα emission in the LAMOST spectrum of KIC 4929016. Lines and symbols are as in Fig. 12.

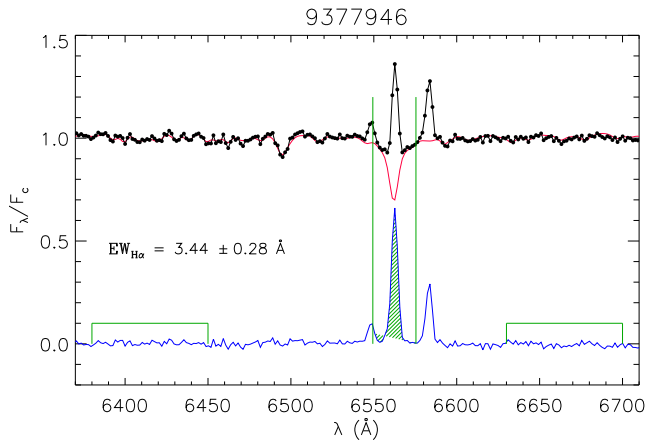

Fig. 14. Example of a star where the Hα line is dominated by nebular sky emission superimposed on the stellar spectrum. The forbidden nitrogen lines at the two sides of Hα appear both in the original and subtracted spectrum.

is known to display a strong and nearly continuous flare activity from the *Kepler* light curves analyzed by Walkowicz et al. (2011).

We selected a total of 577 spectra of 547 stars displaying Hα in emission or filled in by a minimum amount as defined above. The values of $EW_{\rm H\alpha}$, along with their errors, are quoted in Table A.4. We also report whether the line is observed as a pure emission feature and whether the measure is uncertain as a result of the low S/N or other possible spectral issues.

For these stars we also investigated the behavior of the Ca II IRT by subtracting the same inactive template used for the Hα (see lower panels of Figs. 12 and 13). For late-type active stars, the emission, which fills the cores of the Ca II lines, originates from a chromosphere. The equivalent widths of the residual Ca II IRT emission lines, $EW^{\rm res}_{8498}$, $EW^{\rm res}_{8542}$, and $EW^{\rm res}_{8662}$, are also given in Table A.4.

In some cases we saw two emission lines at the two sides of the Hα emission that are, without any doubt, the forbidden lines [N II] at λ 6548 and λ 6584 Å. This pattern is best observed in the residual spectrum (see Fig. 14). These lines are normally observed in ionization nebulae. We think that these emission features can be the result of nebular emission that has not been fully removed by the sky subtraction. Indeed, the intensity of nebular emission was observed to be strongly variable over small spatial scales, from arcminutes down to a few arcseconds (e.g., O'Dell et al. 2003; Hillenbrand et al. 2013), and the sky fibers cannot reproduce the actual nebular emission around each star

in the LAMOST field of view. We also flagged these stars in Table A.4.

4. Chromospheric activity

For stars cooler than about 6500 K, for which the subphotospheric convective envelopes are deep enough to permit an efficient dynamo action, the Hα and Ca II cores are suitable diagnostics of magnetic activity. The best indicators of chromospheric activity, rather than the EW of a chromospheric line, are the surface line flux, F, and the ratio between the line luminosity and bolometric luminosity, R', which are calculated, for the Hα, as

$$F_{\mathrm{H}\alpha} = F_{6563} EW^{\mathrm{res}}_{\mathrm{H}\alpha} \quad (3)$$

$$R'_{\mathrm{H}\alpha} = L_{\mathrm{H}\alpha}/L_{\mathrm{bol}} = F_{\mathrm{H}\alpha}/(\sigma T^4_{\mathrm{eff}}), \quad (4)$$

where F_{6563} is the continuum surface flux at the Hα center, which has been evaluated from the NextGen synthetic low-resolution spectra (Hauschildt et al. 1999) at the stellar temperature and surface gravity of the target. The line fluxes in the three Ca II IRT lines were calculated with similar relations, where the continuum flux at the center of each line was also evaluated from the NextGen spectra. For each line, the flux error includes both the EW error and uncertainty in the continuum flux at the line center, which is obtained by propagating the T_{eff} and $\log g$ errors.

The Hα fluxes and $R'_{\mathrm{H}\alpha}$ of our targets are plotted as a function of the effective temperature in Fig. 15, along with the boundary between the accreting objects (mostly located above this line) and the chromospherically active stars, as defined by Frasca et al. (2015). Different symbols are used for stars with solid measures of $EW^{\mathrm{res}}_{\mathrm{H}\alpha}$ (blue dots) and those where the detection of the Hα core filling is less secure (green asterisks) either because of a low S/N, problems in the spectrum, or the presence of nebular emission lines. This figure clearly shows a different lower level of fluxes and R' for stars with $T_{\mathrm{eff}} < 5000$ K and $T_{\mathrm{eff}} > 5000$ K, which is the result of the two thresholds adopted for selecting active stars in the two T_{eff} domains.

We point out that only one star is located in the region occupied by accreting stars. This object, KIC 8749284, is denoted with "1" in Fig. 15b. It was classified by ROTFIT as K1 V and it is the star with the highest value of $EW^{\mathrm{res}}_{\mathrm{H}\alpha}$ (13 Å). In the only spectrum acquired by LAMOST there is no clear evidence of lithium absorption, which is normally observed in young accreting objects. Alternatively, this object could be an active close binary (SB2 or SB1) composed of main-sequence or evolved stars. Nevertheless, a young age is supported by the infrared (IR) colors, which place KIC 8749284 in the domain of Class II objects in the 2MASS and WISE color-color diagrams (e.g., Koenig et al. 2012). Besides, the spectral energy distribution (SED) clearly shows an IR excess starting from the H band, which is compatible with an evolved circumstellar disk of a Class II source (see Fig. 16). The fit of the SED has been performed as in Frasca et al. (2015) from the B to J band, adopting the effective temperature found by ROTFIT for the photospheric model and letting the interstellar extinction A_V free to vary. This star displays rotational modulation in the *Kepler* photometry with a period of about 3.2 days (Debosscher et al. 2011). Follow-up spectroscopic observations with a higher resolution would help to unveil its nature.

The star labeled "2", which lies close to the dividing line in Fig. 15, is KIC 8991738. Its SED does not show any IR excess (Fig. 16). Although it is included in the KIC, it has never been observed by *Kepler*. The target "3", KIC 4644922 (=V677 Lyr), has an anomalously high level of chromospheric activity for such a hot star. It was previously classified as a semiregular variable (e.g., Pigulski et al. 2009). Indeed, according to Gorlova et al. (2012), KIC 4644922 is a candidate post-AGB star surrounded by a dusty disk for which the Hα emission originates in the circumstellar environment. The spectra of star "4" (KIC 8722673) and "5" (KIC 9377946) show the clear pattern of nebular emission with the two forbidden nitrogen lines at the two sides of Hα (see Fig. 14 for KIC 9377946). We think that, for these two stars, the strong Hα flux does not have a chromospheric origin but is mostly the result of sky line emission that overlaps the stellar spectrum.

In Fig. 17 we compare the Hα and Ca II chromospheric fluxes. The latter, $F_{\mathrm{CaII-IRT}}$, is the sum of the flux in each line of the triplet. We limited our analysis to the GKM stars ($T_{\mathrm{eff}} < 6000$ K) to minimize the contamination by sources for which the emission does not have a chromospheric origin. However, this subsample (442 stars) is a large portion of the sample of active objects that were selected as described in Sect. 3.4. The two fluxes are clearly correlated, as indicated by the Spearman's rank correlation coefficient $\rho = 0.62$ with a significance of $\sigma = 4.35 \times 10^{-24}$ (Press et al. 1992). A least-squares regression yields the following relation:

$$\log F_{\mathrm{H}\alpha} = -1.85 + 1.25 \cdot \log F_{\mathrm{CaII-IRT}}, \quad (5)$$

where we took the bisector of the two least-squares regressions (X on Y and Y on X). A power law with an exponent larger than 1 for this flux–flux relationship is in agreement with previous results (see, e.g., Martínez-Arnáiz et al. 2011, and reference therein).

For about 200 stars we found the rotation periods in the literature (Debosscher et al. 2011; Nielsen et al. 2013; Reinhold et al. 2013; McQuillan et al. 2013, 2014; Mazeh et al. 2015). We found that, besides the scatter, the Hα flux increases with decreasing rotation period, P_{rot}, as shown in Fig. 18. The correlation with P_{rot} is an expected result, based on the $\alpha\Omega$ dynamo mechanism, and it is widely documented in the literature for several diagnostics of chromospheric and coronal activity (e.g., Frasca & Catalano 1994; Montes et al. 1995; Pizzolato et al. 2003; Cardini & Cassatella 2007; Reiners et al. 2015, and references therein). The Spearman rank correlation analysis, which is limited to the stars with solid measures of Hα emission (blue dots in Fig. 18) and $T_{\mathrm{eff}} < 6000$ K, yields a correlation coefficient $\rho = -0.59$ with a significance of $\sigma = 2.5 \times 10^{-11}$, which means a highly significant correlation between $F_{\mathrm{H}\alpha}$ and P_{rot}. A similar behavior, albeit with a lower degree of correlation ($\rho = -0.18$; $\sigma = 0.07$), is displayed by the Ca II-IRT flux. We think that the low resolution of the spectra, which gives rise to rather large flux errors, and the heterogeneous sample, which includes stars with very different properties, are mainly responsible for the large data scatter. The latter prevents us, for example, from clearly distinguishing the saturated and unsaturated activity regimes.

5. Summary

We are carrying out a large spectroscopic survey of the stars in the *Kepler* field using the LAMOST spectrograph. In this paper we present the results of the analysis of the spectra obtained during the first round of observations (2011–2014), which are mainly based on the code ROTFIT.

We selected spectra with Hα emission and chromospherically active stars by means of the spectral subtraction of inactive

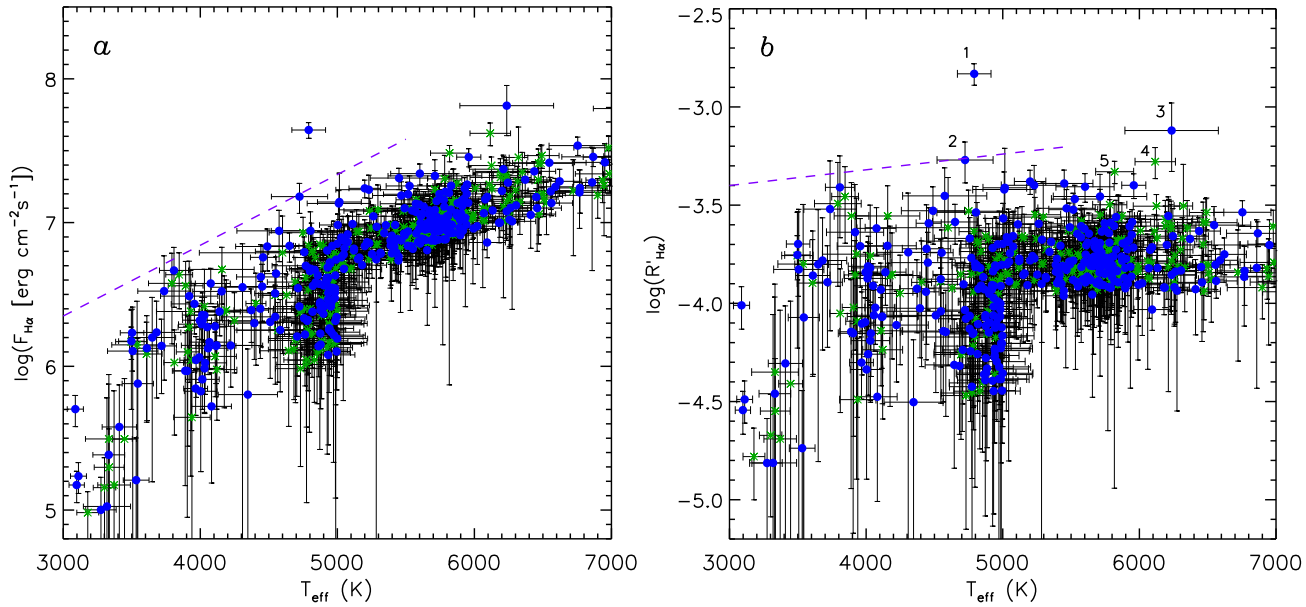

Fig. 15. *Left panel*: Hα flux vs. $T_{\rm eff}$. *Right panel*: $R'_{\rm H\alpha}$ vs. $T_{\rm eff}$. In both panels the candidates with a questionable emission are denoted with green asterisks. The dashed straight line is the boundary between chromospheric emission (below it) and accretion as derived by Frasca et al. (2015).

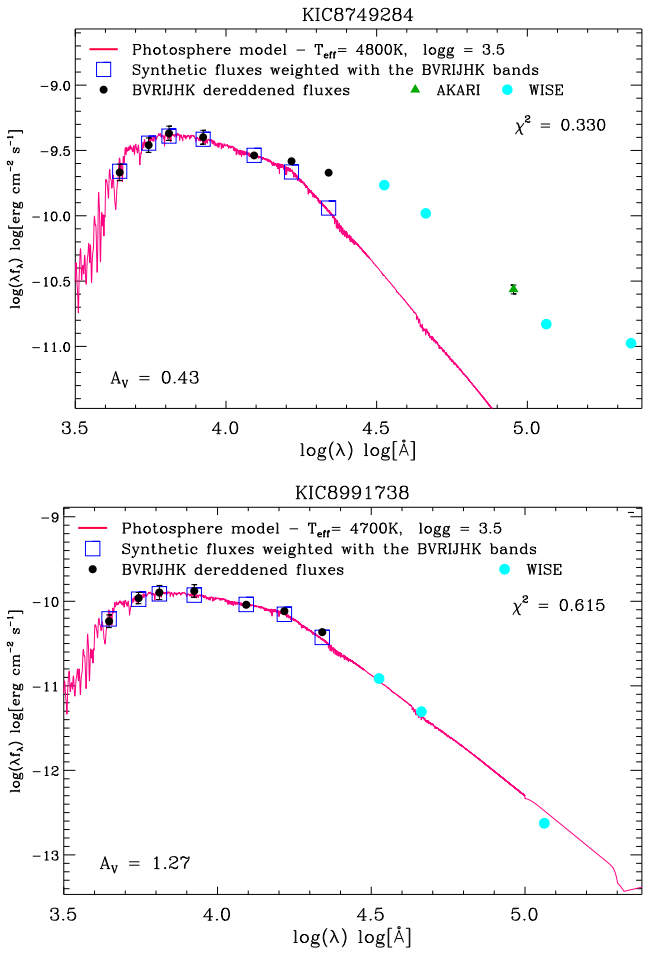

Fig. 16. Spectral energy distribution of the two stars cooler than 5500 K with the highest $R'_{\rm H\alpha}$ values. Note the IR excess for KIC 8749284.

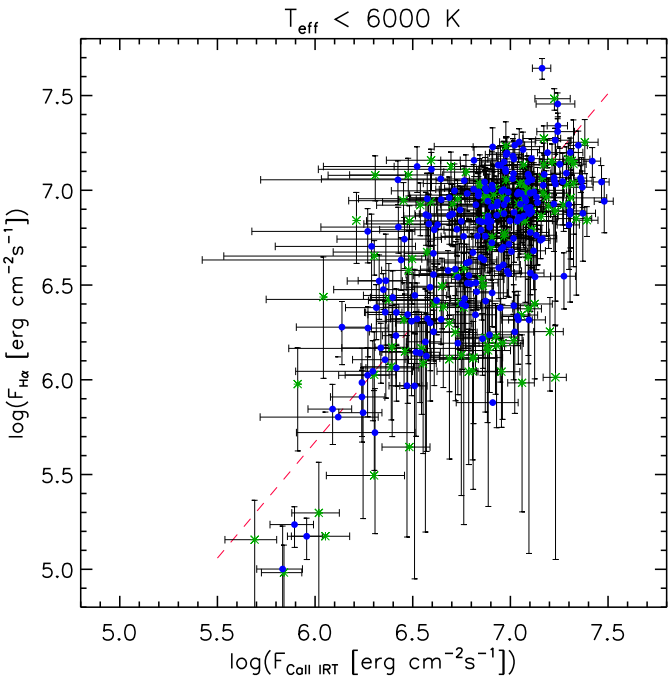

Fig. 17. Flux–flux relationship between Hα and Ca II IRT. The meaning of the symbols is as in Fig. 15. The dashed line is the least-squares regression.

templates chosen in a large grid of real-star spectra. Because of the low resolution and rather low S/N for most of the surveyed stars, we set an *EW* threshold that minimizes the contamination with false positive detections. For cool stars ($T_{\rm eff}$ < 6000 K) we also calculated the Hα and Ca II-IRT fluxes, which are important proxies of chromospheric activity.

In total, we analyzed 61 753 spectra of 51 385 stars performing an MK spectral classification, evaluating their atmospheric parameters ($T_{\rm eff}$, log g, and [Fe/H]) and deriving their radial velocity (RV). Our code also allows us to measure the projected rotation velocity ($v \sin i$) that, because of the low resolution of the LAMOST spectra, is possible only for fast-rotating stars ($v \sin i > 120\,{\rm km\,s^{-1}}$).

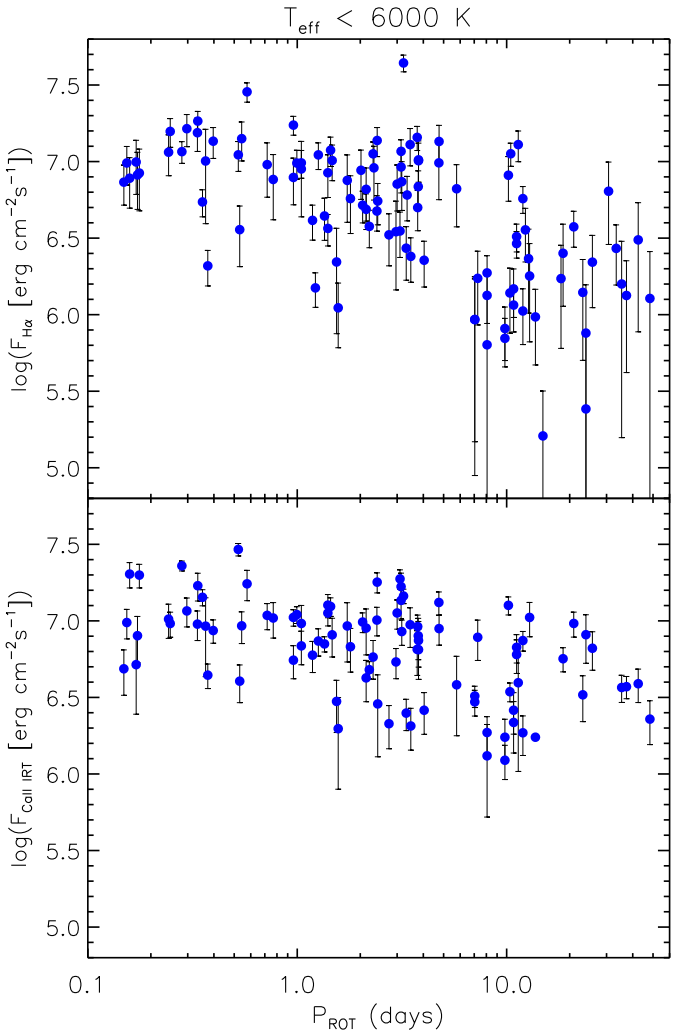

Fig. 18. Hα and Ca II-IRT flux vs. $P_{\rm rot}$.

To check the data quality, we searched in the literature for values of the parameters derived from high- or intermediate-resolution spectra. The comparison of the LAMOST $T_{\rm eff}$ values with those from the literature (468 stars in the range 3000–20 000 K) shows a very good agreement and indicates an accuracy of about 3.5%. The comparison with literature values for $\log g$ (352 stars) displays a larger scatter and the tendency of LAMOST values to cluster around the average $\log g$ of main-sequence stars (∼4.5) and red giants (∼2.5). Similarly, for [Fe/H] we found a systematic trend, which is best observed when our data are compared with those from the APOKASC catalog (787 stars in common). We proposed a correction relation for the metallicities derived with ROTFIT from the LAMOST spectra, which is based on these comparisons. These effects are likely the result of both the low resolution and the uneven distributions of the spectral templates in the space of parameters. Anyway, the accuracy of the $\log g$ and [Fe/H] measurements is sufficient to perform a discrete luminosity classification and to sort the stars in bins of metallicity. This allows us to get a safe flux calibration of the lines EWs.

Our RV measurements agree with literature data within 14 km s^{-1} , which we consider the external accuracy. Despite the rather low LAMOST resolution, we could identify interesting and peculiar objects, such as stars with variable RV (SB or pulsating star candidates), ultrafast rotators, and stars in particular evolutionary stages.

Our data display a different metallicity distribution compared to that obtained from the Sloan photometry, with a median value that is higher by about 0.15 dex. This result is in agreement with previous findings based on smaller data samples, supporting the validity of the correction relation for [Fe/H] that we proposed.

The RV distribution is asymmetric and shows an excess of stars with negative RVs which is larger at low metallicities. This results is in agreement with the data of the SEGUE survey in the *Kepler* field.

Based on the Hα and Ca II-IRT fluxes, we have found 442 chromospherically active stars, one of which is a likely accreting object, as indicated by the strong and broad Hα emission and by the relevant infrared excess. The availability of precise rotation periods from the *Kepler* photometry has allowed us to study the dependency of these chromospheric fluxes on the rotation rate for a very large sample of field stars. We found that both the Hα and Ca II-IRT fluxes are correlated with the rotation period, with the former diagnostic showing the largest decrease with the increasing $P_{\rm rot}$.

Acknowledgements. The authors are grateful to the anonymous referee for very useful suggestions. Guoshoujing Telescope (the Large Sky Area Multi-Object Fibre Spectroscopic Telescope LAMOST) is a National Major Scientific Project built by the Chinese Academy of Sciences. Funding for the project has been provided by the National Development and Reform Commission. lamost is operated and managed by the National Astronomical Observatories, Chinese Academy of Sciences. We thank Katia Biazzo and Gijs Mulders for helpful discussions and suggestions. Support from the Italian *Ministero dell'Istruzione, Università e Ricerca* (MIUR) is also acknowledged. J.M.-Ż. acknowledges the funding received from the European Community's Seventh Framework Programme (FP7/2007–2013) under grant agreement No. 269194 and grant number NCN 2014/13/B/ST9/00902. J.N.F. and A.N.R. acknowledge the support of the Joint Fund of Astronomy of National Natural Science Foundation of China (NSFC) and Chinese Academy of Sciences through the Grant U1231202, and the National Basic Research Program of China (973 Program 2014CB845700 and 2013CB834900). Y.W. acknowledges the National Science Foundation of China (NSFC) under grant 11403056. This research made use of SIMBAD and VIZIER databases, operated at the CDS, Strasbourg, France. This publication makes use of data products from the Two Micron All Sky Survey, which is a joint project of the University of Massachusetts and the Infrared Processing and Analysis Center/California Institute of Technology, funded by the National Aeronautics and Space Administration and the National Science Foundation. This publication makes use of data products from the Wide-field Infrared Survey Explorer, which is a joint project of the University of California, Los Angeles, and the Jet Propulsion Laboratory/California Institute of Technology, funded by the National Aeronautics and Space Administration.

References

Abt, H. A., & Morrel, N. I. 1995, ApJS, 99, 135
Abt, H. A., Levato, H., & Grosso, M. 2002, ApJ, 573, 359
Allende Prieto C., et al. 2008, Astron. Nachr., 329, 1018
Balona, L. A., Pigulski, A., De Cat, P., et al. 2011, MNRAS, 413, 2043
Barbier-Brossat, M., Petit, M., & Figon, P. 1994, A&AS, 108, 603
Batalha, N. M., Rowe, J. F., Bryson, S. T., et al. 2013, ApJS, 204, 24
Bevington, P. 1969, in Data Reduction and Error Analysis for the Physical Sciences (New York: Mc Graw-Hill), 237
Brown, T. M., Latham, D. W., Everett, M. E., & Esquerdo, G. A. 2011, AJ, 144, 24
Bruntt, H., Frandsen, S., & Thygesen, A. O. 2011, A&A, 528, A121
Bruntt, H., Basu, S., Smalley, B., et al. 2012, MNRAS, 423, 122
Buchhave, L. A., Latham, D. W., Johansen, A., et al. 2012, Nature, 486, 375
Cardini, D., & Cassatella, A. 2007, ApJ, 666, 393
Casagrande, L., Schönrich, R., Asplund, M., et al. 2011, A&A, 530, A138
Casagrande, L., Silva Aguirre, V., Stello, D., et al. 2014, ApJ, 787, 110
Casagrande, L., Silva Aguirre, V., Schlesinger, K. J., et al. 2016, MNRAS, 455, 987
Catanzaro, G., Frasca, A., Molenda-Żakowicz, J., & Marilli, E. 2010, A&A, 517, A3
Catanzaro, G., Ripepi, V., Bernabei, S., et al. 2011, MNRAS, 411, 1167
Debosscher, J., Blomme, J., Aerts, C., & De Ridder, J. 2011, A&A, 529, A89
De Cat, P., Fu, J. N., Ren, A. B., et al. 2015, ApJS, 220, 19 (Paper I)
Delfosse, X., Forveille, T., Perrier, C., & Mayor, M. 1998, A&A, 331, 581

Deshpande, R., Blake, C. H., Bender, C. F., et al. 2013, AJ, 146, 156
de Medeiros, J. R., & Mayor, M. 1999, A&AS, 139, 433
Dong, S., Zheng, Z., Zhu, Z., et al. 2014, ApJ, 789, L3
Famaey, B., Jorissen, A., Luri, X., et al. 2005, A&A, 430, 165
Fehrenbach, C., Duflot, M., Mannone, C., Burnage, R., & Genty, V. 1997, A&AS, 124, 255
Fekel, F. C. 1997, PASP, 109, 514
Frasca, A., & Catalano, S. 1994, A&A, 284, 883
Frasca, A., Alcalá, J. M., Covino, E., et al. 2003, A&A, 405, 149
Frasca, A., Guillout, P., Marilli, E., et al. 2006, A&A, 454, 301
Frasca, A., Fröhlich, H.-E., Bonanno, A., et al. 2011, A&A, 523, A81
Frasca, A., Biazzo, K., Lanzafame, A. C., et al. 2015, A&A, 575, A4
Frinchaboy, P. M., & Majewski, S. R. 2008, AJ, 136, 118
Fröhlich, H.-E., Frasca, A., Catanzaro, G., et al. 2011, A&A, 543, A146
Fukugita, M., Ichikawa, T., Gunn, J. E., et al. 1996, AJ, 111, 1748
Gilmore, G., et al. 2012, Messenger, 147, 25
Gontcharov, G. A. 2006, Astron. Lett., 32, 759
Gorlova, N., Van Winckel, H., & Jorissen, A. 2012, Balt. Astron., 21, 165
Gray, D. F., & Toner, C. G. 1987, ApJ, 322, 360
Gray, R. O., Corbally, C. J., De Cat, P., et al. 2016, AJ, 151, 13
Grenier, S., Baylac, M.-O., Rolland, L., et al. 1999, A&AS, 137, 451
Hauck, B., & Mermilliod, M. 1998, A&AS, 129, 431
Hauschildt, P. H., Allard, F., & Baron, E. 1999, ApJ, 512, 377
Hillenbrand, L. A., Hoffer, A. S., & Herczeg, G. J. 2013, AJ, 146, 85
Howarth, I. D., Siebert, K. W., Hussain, G. A. J., & Prinja, R. K. 1997, MNRAS, 284, 265
Hubble E. 1942, Science, 95, 212
Huber, D., Chaplin, W. J., Christensen-Dalsgaard, J., et al. 2013, ApJ, 767, 127
Huber, D., Silva Aguirre, V., Matthews, J. M., et al. 2014, ApJS, 211, 2
Jackson, R. J., Jeffries, R. D., Lewis, J., et al. 2015, A&A, 580, A75
Kepler, J. 1609, Astronomia nova
Kharchenko, N. V., Scholz, R.-D., Piskunov, A. E., Röser, S., & Schilbach, E. 2007, Astron. Nachr., 328, 889
Koenig, X. P., Leisawitz, D. T., Benford, D. J., et al. 2012, ApJ, 744, 130
Lehmann, H., Tkachenko, A., Semaan, T., et al. 2011, A&A, 526, A124
Linsky, J. R., Hunten, D. M., Sowell, R., Glackin, D. L., & Kelch, W. L. 1979, ApJS, 41, 481
Luo A.-L., Zhang, H.-T., Zhao, Y.-H., et al. 2012, RA&A, 12, 1243
Luo, A.-L., Zhao, Y.-H., Zhao, G., et al. 2015, RA&A, 15, 1095
Mann, A. W., Gaidos, E., Lépine, S., & Hilton, E. J. 2012, ApJ, 753, 90
Marcy, G. W., Isaacson, H., Howard, A. W., et al. 2014, ApJS, 210, 20
Martínez-Arnáiz, R., López-Santiago, J., Crespo-Chacón, I., & Montes, D., MNRAS, 414, 2629
Mazeh, T., Perets, H. B., McQuillan, A., & Goldstein, E. S. 2015, ApJ, 801, 3
McNamara, B. J., Jackiewicz, J., & McKeever, J. 2012, AJ, 143, 101
McQuillan, A., Mazeh, T., & Aigrain, S. 2013, ApJ, 775, L11
McQuillan, A., Mazeh, T., & Aigrain, S. 2014, ApJS, 211, 24
Mermilliod, J. C., Mayor, M., & Udry S. 2008, A&A, 485, 303
Meszaros, Sz., Holtzman, J., Garcia Perez, A. E., et al. 2013, AJ, 146, 133
Molenda-Żakowicz, J., Frasca, A., Latham, D. W., & Jerzykiewicz, M. 2007, Acta Astron., 57, 301
Molenda-Żakowicz, J., Frasca, A., & Latham, D. W. 2008, Acta Astron., 58, 419
Molenda-Żakowicz, J., Latham, D. W., Catanzaro, G., Frasca, A., & Quinn, S. N. 2011, MNRAS, 412, 1210
Molenda-Żakowicz, J., Sousa, S. G., Frasca, A., et al. 2013, MNRAS, 434, 1422
Molenda-Żakowicz, J., Brogaard, K., Niemczura, E., et al. 2014, MNRAS, 445, 2446
Montes, D., Fernández-Figueroa, M. J., De Castro, E., & Cornide, M. 1995, A&A, 294, 165
Nidever, D. L., Marcy, G. W., Butler, R. P., Fischer, D. A., & Vogt, S. S. 2002, ApJS, 141, 503
Nielsen, M. B., Schunker, H., Gizon, L., & Ball, W. H. 2015, A&A, 582, A10
Niemczura, E., Murphy, S. J., Smalley, B., et al. 2015, MNRAS, 450, 2764
Nordström, B., Mayor, M., Andersen, J., et al. 2004, A&A, 418, 989
Norton, R. M. 1984, The American Statistician (American Statistical Association), 38, 135
O'Dell, C. R., Peimbert, M., & Peimbert, A. 2003, AJ, 125, 2590
Pakhomov, Yu. V., Antipova, L. I., Boyarchuk, A. A., Zhao, G., & Liang, Ya. 2009, Astron. Rep., 53, 685
Petigura, E. A., Marcy, G. W., & Howard, A. W. 2013, ApJ, 770, 69
Pigulski, A., Pojmański, G., Pilecki, B., & Szczygieł, D. M. 2009, Acta Astron., 59, 33
Pinsonneault, M. H., Elsworth, Y., Epstein, C., et al. 2014, ApJS, 215,
Pizzolato, N., Maggio, A., Micela, G., Sciortino, S., & Ventura, P. 2003, A&A, 397, 147
Pojmański, G. 1997, Acta Astron., 47, 467
Press, W. H., Teukolsky, S. A., Vetterling, W. T., & Flannery, B. P. 1992, Numerical Recipes in Fortran 2nd edn. (Cambridge: Cambridge Univ. Press)
Queloz, D., Allain, S., Mermilliod, J.-C., Bouvier, J., & Mayor, M. 1998, A&A, 335, 183
Reiners, A., Schüssler, M., & Passegger, V. M. 2014, ApJ, 794, 144
Reinhold, T., Reiners, A., & Basri, G. 2013, A&A, 560, A4
Ren, A. B., Fu, J. N., De Cat, P., et al. 2016, ApJS, submitted
Royer, F., Grenier, S., Baylac, M.-O., Gómez, A. E., & Zorec, J. 2002, A&A, 393, 897
Saar, S. H., & Osten, R. A. 1997, MNRAS, 284, 803
Shapley, H., & Curtis, H. D. 1921, Bulletin of the National Research Council, 2, 171
Steinmetz, M., et al. 2006, AJ, 132, 1645
Thygesen, A. O., Frandsen, S., Bruntt, H., et al. 2012, A&A, 543, A160
Tkachenko, A., Lehmann, H., Smalley, B., Debosscher, J., & Aerts, C. 2012, MNRAS, 422, 2960
Torres, G., Fischer, D. A., Sozzetti, A., et al. 2012, ApJ, 757, 161
Tucker, D. L., Kent, S., Richmond, M. W., et al. 2006, Astron. Nachr., 327, 821
Udalski, A., Szymanski, M., Kałużny, J., Kubiak, M., & Mateo, M. 1992, Acta Astron., 42, 253
Uytterhoeven, K., Briquet, M., Bruntt, H., et al. 2010, Astron. Nachr., 331, 993
Uytterhoeven, K., Moya, A., Grigahcène, et al. 2011, A&A, 534, A125
Valdes, F., Gupta, R., Rose, J. A., Singh, H. P., & Bell, D. J. 2004. ApJS, 152, 251
Walkowicz, L. M., Basri, G., Batalha, N., et al. 2011, AJ, 141, 50
Wang, S.-G., Su, D.-Q., Chu, Y.-Q., Cui, X., & Wang, Y.-N. 1996, Apl. Opt., 35, 5155
Wang, J., Fischer, D. A., Barclay, T., et al. 2013, ApJ, 776, 10
Wilson, R. E. 1953, in General Catalogue of Stellar Radial Velocities (Carnegie Inst. Washington D.C. Publ.), 601
Wu, Y., Singh, H. P., Prugniel, P., Gupta, R., & Koleva, M. 2011, A&A, 525, A71
Wu, Y., Du, B., Luo, A., Zhao, Y., & Yuan, H. 2014, in Statistical Challenges in 21st Century Cosmology, Proc. IAU Symp., 306, 340
Xing, X., Zhai, C., Du, H., et al. 1998, Proc. SPIE, 3352, 839
Yanny, B., Rockosi, C., Newberg, H. J., et al. 2009, AJ, 137, 4377
York D. G., et al. 2000, AJ, 120, 1579
Zhao, G., Zhao, Y.-H., Chu, Y.-Q., Jing, Y.-P., & Deng, L.-C. 2012, RA&A, 12, 723

Appendix A: Additional data

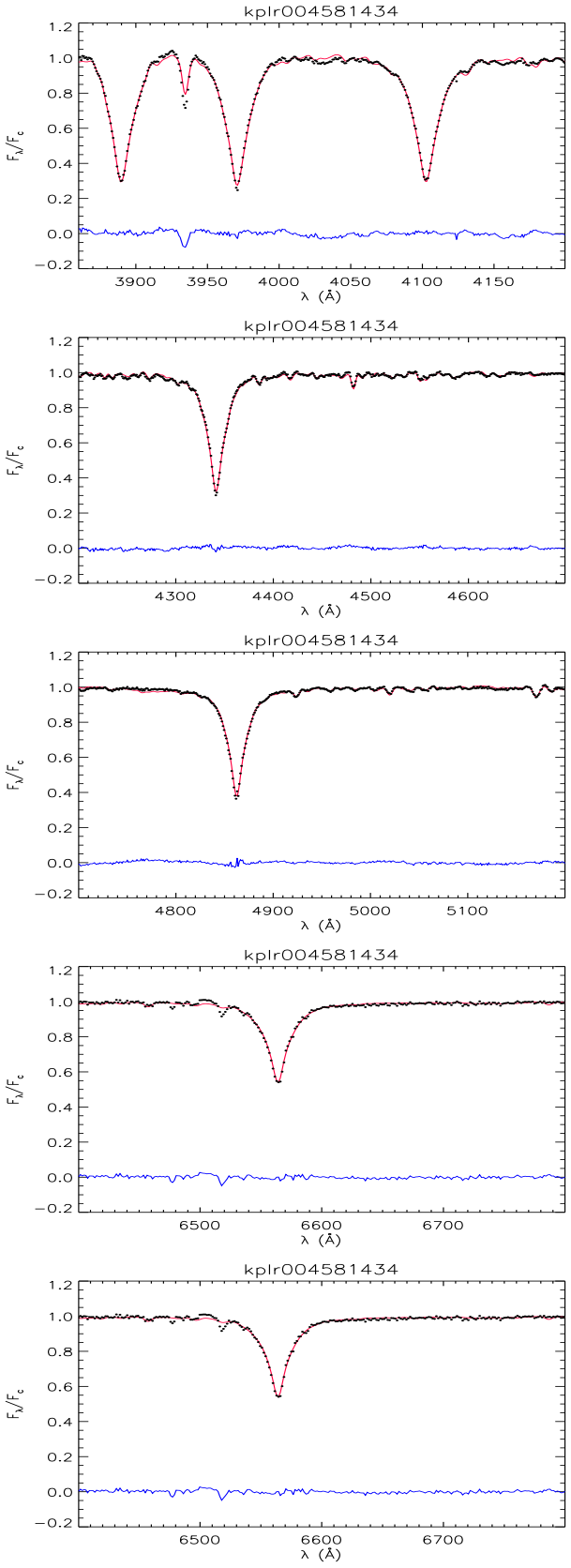

Fig. A.1. Example of the continuum-normalized LAMOST spectrum of an early A-type star in five spectral regions (dots). The best template found by ROTFIT is overplotted with a thin red line. The difference between the two spectra is shown in the bottom of each panel with a blue full line.

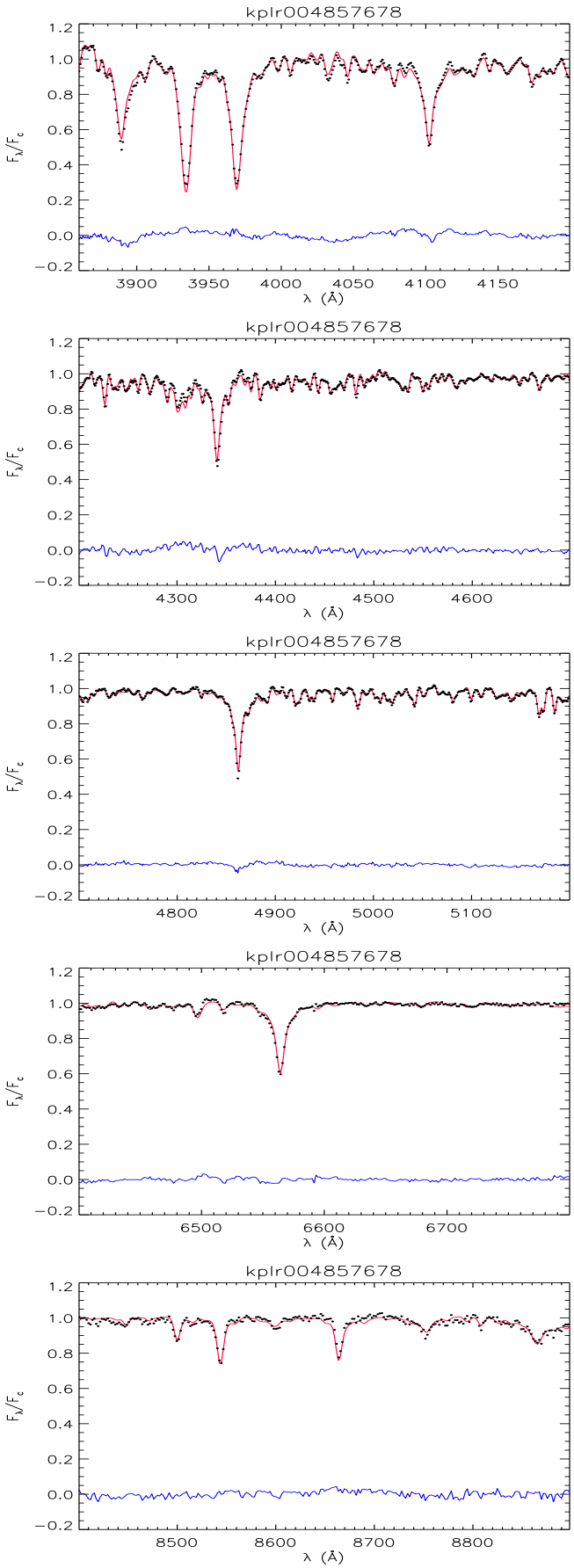

Fig. A.2. Same as Fig. A.1 but for an F5 V star.

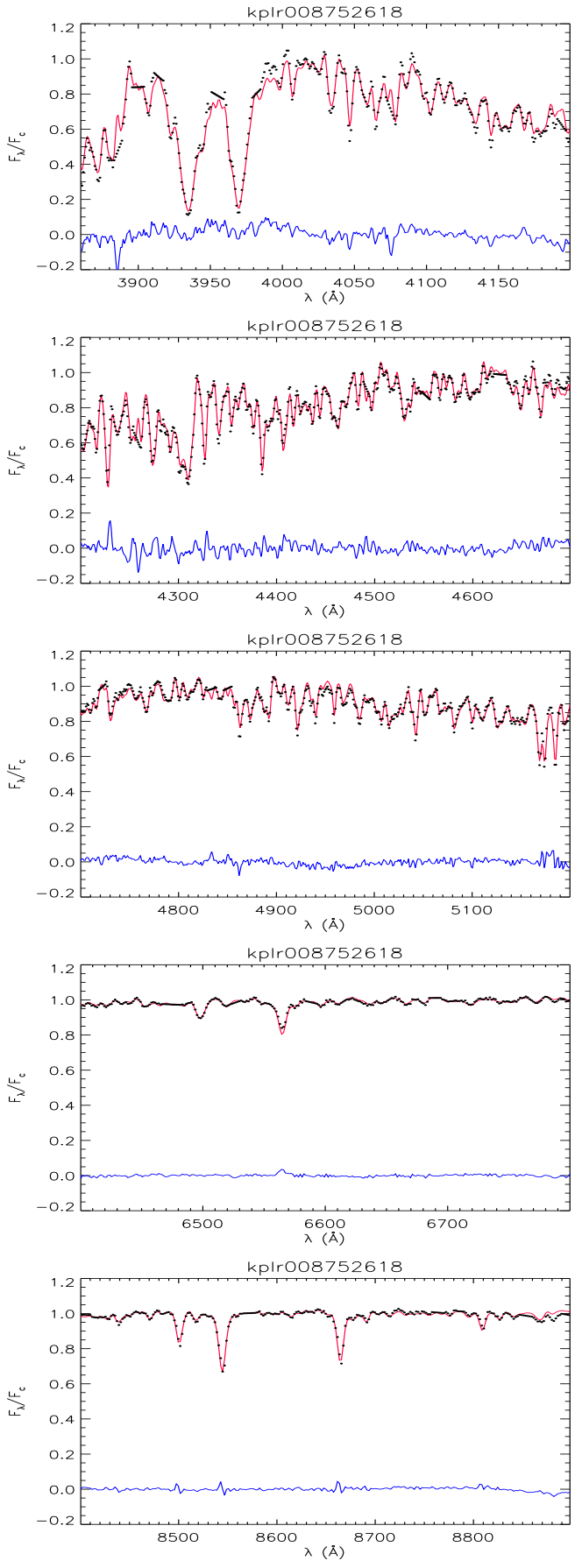

Fig. A.3. Same as Fig. A.1 but for a K0 III star.

Table A.1. Stars with radial velocity in the literature.

KIC	Name	HJD (−2 400 000)	RV_{LAM} (km s^{-1})	σ_{RV}^{LAM}	RV_{Lit} (km s^{-1})	σ_{RV}^{Lit}	Reference
1 726 211	TYC 2667-624-1	56 094 .21294	−129.1	17.3	−145.80	...	T12
1 861 900	HD 181 655	56 094 .25369	−19.0	21.0	2.03	0.09	N02
1 873 543	2MASS J19302029+3723437	56 094 .29879	12.3	21.6	23.06	0.35	D13
2 425 631	TYC 3120-1300-1	56 811 .25084	32.9	17.8	19.10	...	T12
2 837 475	HD 179 260	55 721 .30256	−5.6	29.4	−13.00	0.70	N04
3 430 868	HD 179 306	55 721 .30252	22.6	25.2	5.40	...	T12
3 563 082	HD 186 506	56 096 .24488	−14.5	18.3	−22.10	0.30	G06
3 657 793	HD 185 562	56 096 .27008	−15.7	19.8	-0.44	0.42	F05
3 748 585	BD+38 3601	56 096 .26934	−0.5	18.3	−5.80	...	T12
3 748 691	TYC 3134-261-1	56 096 .26934	2.9	20.0	−0.10	...	T12
3 860 139	TYC 3135-696-1	56 096 .26924	−2.4	18.3	−25.20	...	T12
3 955 590	TYC 3134-31-1	56 096 .24501	−49.6	18.0	−57.20	...	T12
4 070 746	TYC 3135-326-1	56 096 .26919	9.5	19.3	−1.60	...	T12
4 161 741	HIP 95 913	56 096 .26927	−21.6	20.4	−22.84	0.16	M08
4 177 025	TYC 3136-647-1	56 096 .24579	−87.0	16.8	−123.10	...	T12
4 242 575	HD 176 845	55 721 .30254	−19.2	19.2	−32.30	2.80	N04
4 283 484	HD 225 666	56 096 .27009	−23.5	17.4	−44.80	...	T12
4 283 484	HD 225 666	56 570 .97671	−52.1	16.3	−44.80	...	T12
4 283 484	HD 225 666	56 800 .32810	−18.0	19.1	−44.80	...	T12
4 352 924	HD 179 733	56 094 .22092	−5.1	24.8	−18.50	2.50	G06
4 352 924	HD 179 733	55 721 .28765	10.6	23.6	−18.50	2.50	G06
4 484 238	HIP 97 236	56 096 .27008	−6.9	19.0	−14.78	0.34	M11
4 574 610	HIP 96 775	56 096 .24482	−31.5	24.0	−44.52	0.45	M11
4 581 434	HD 186 997	56 096 .24574	−0.3	28.6	−4.30	6.20	C10
4 581 434	HD 186 997	56 570 .97672	−13.5	25.4	−4.30	6.20	C10
4 581 434	HD 186 997	56 800 .32808	39.2	38.6	−4.30	6.20	C10
4 659 706	TYC 3139-1785-1	56 096 .26918	−10.0	16.4	−21.80	...	T12
4 914 923	BD+39 3706	56 094 .22083	−51.0	19.8	−25.46	1.01	M07
4 929 016	2MASS J19330692+4005066	56 096 .26915	−11.5	15.6	−20.10	0.07	D13
5 113 061	TYC 3140-2350-1	56 096 .26908	24.6	18.0	−4.30	...	T12
5 113 910	2MASS J19421943+4016074	56 096 .30212	18.5	16.3	−12.40	...	T12
5 206 997	HIP 97 337	56 096 .27060	−56.6	27.2	−70.50	0.49	M07
5 206 997	HIP 97 337	56 570 .97674	−78.9	16.2	−70.50	0.49	M07
5 206 997	HIP 97 337	56 800 .32802	−59.9	20.4	−70.50	0.49	M07
5 284 127	TYC 3139-1918-1	56 570 .97656	−73.1	16.8	−73.00	...	T12
5 442 047	HIP 94 952	56 094 .25340	−54.5	21.1	−53.92	0.18	M08
5 511 423	2MASS J18523459+4046480	56 572 .95996	−109.7	18.0	−87.30	...	T12
5 524 720	2MASS J19160889+4044237	56 094 .21277	−46.5	23.1	−32.80	...	T12
5 524 720	2MASS J19160889+4044237	56 562 .00867	−38.9	15.9	−32.80	...	T12
5 612 549	TYC 3125-195-1	56 094 .25339	−11.0	20.0	−3.50	...	T12
5 612 549	TYC 3125-195-1	56 562 .00870	−12.3	15.3	−3.50	...	T12
5 701 829	BD+40 3689	56 432 .26132	1.3	16.0	−20.50	...	T12
5 709 564	TYC 3139-1534-1	56 094 .21261	−79.4	21.2	−104.90	...	T12
5 786 771	HD 182 192	56 432 .26132	21.7	23.7	−21.70	12.10	C10
5 792 581	TYC 3138-169-1	56 094 .21263	−2.5	20.4	5.20	...	T12
5 859 492	TYC 3124-1301-1	55 721 .28761	−37.1	27.1	−59.40	...	T12
6 289 468	BD+41 3389	56 096 .25166	3.3	34.7	0.51	0.42	Tk12
6 289 468	BD+41 3389	56 562 .01362	−13.4	22.0	0.51	0.42	Tk12
6 579 998	TYC 3126-920-1	56 572 .95987	−58.4	15.2	−43.40	...	T12
6 680 734	TYC 3129-1020-1	56 432 .26135	26.9	16.3	12.60	...	T12
6 696 436	BD+41 3390	56 096 .24467	−19.8	22.8	−13.90	...	T12

Notes. B94 = Barbier-Brossat et al. (1994); C10 = Catanzaro et al. (2010); D13 = Deshpande et al. (2013); F05 = Famaey (2005); F08 = Frinchaboy (2008); F11 = Frasca et al. (2011); F12 = Fröhlich et al. (2012); F97 = Fehrenbach et al. (1997); G06 = Gontcharov (2006); G99 = Grenier et. al. (1999); K07 = Kharchenko et al. (2007); M07 = Molenda-Żakowicz et al. (2007); M08 = Molenda-Żakowicz et al. (2008); M11 = Molenda-Żakowicz et al. (2011); M14 = Molenda-Żakowicz et al. (2014); Me08= Mermilliod et al. (2008); N02 = Nidever et al. (2002); N04 = Nordström et al. (2004); P09 = Pakhomov et al. (2009); T12 = Thygesen et al. (2012); Tk12 = Tkachenko et al. (2012); W53 = Wilson (1953).

Table A.1. continued.

KIC	Name	HJD (−2 400 000)	RV_{LAM} (km s^{-1})	σ_{RV}^{LAM}	RV_{Lit} (km s^{-1})	σ_{RV}^{Lit}	Reference
6 837 256	TYC 3126-801-1	56 572 .95986	−16.1	16.1	0.90	...	T12
6 848 529	BD+42 3250	56 582 .98090	−9.9	18.4	−14.30	3.00	C10
6 976 475	BD+42 3518	56 570 .97685	−37.3	16.2	−31.75	0.34	M07
7 131 828	HIP 96 992	56 083 .27607	7.5	21.9	−14.00	...	B94
7 374 855	HIP 96 846	56 083 .27607	−6.1	17.3	−17.42	0.10	M08
7 456 762	HIP 96 805	56 083 .27606	6.3	41.3	−6.10	0.30	G06
7 599 132	HD 180 757	56 432 .26125	11.6	17.9	−57.20	1.80	C10
7 599 132	HD 180 757	56 570 .00492	−51.5	18.9	−57.20	1.80	C10
7 693 833	TYC 3148-2052-1	56 914 .02679	−19.0	19.6	−14.30	...	T12
7 765 135	TYC 3148-2163-1	56 570 .97662	−27.4	18.3	−20.00	0.20	F12
7 812 552	TYC 3133-2090-1	56 562 .00822	9.5	18.0	16.00	...	T12
7 985 370	HD 189 210	56 561 .00321	−30.6	18.0	−24.00	0.30	F12
8 177 087	HD 186 428	56 083 .27590	18.7	29.3	24.00	18.20	F97
8 228 742	BD+43 3221	56 432 .26115	18.4	17.2	10.41	0.19	M07
8 312 388	HD 186 787	56 083 .27592	−15.3	18.4	−28.00	3.70	F97
8 389 948	HD 189 159	56 561 .00320	−42.7	19.8	−31.70	5.40	C10
8 389 948	HD 189 159	56 561 .04145	−27.0	20.0	−31.70	5.40	C10
8 389 948	HD 189 159	56 582 .98090	−33.0	20.9	−31.70	5.40	C10
8 389 948	HD 189 159	56 590 .96202	−37.9	21.6	−31.70	5.40	C10
8 429 280	TYC 3146-35-1	56 432 .26113	−16.5	16.0	−33.10	0.50	F11
8 491 147	BD+44 3110	56 432 .26112	20.4	16.1	7.10	...	T12
8 493 969	TYC 3146-242-1	56 432 .26113	7.6	16.1	−9.50	...	T12
8 504 443	HD 186 140	56 083 .27595	−16.7	21.5	−25.00	0.30	G06
8 539 201	BD+44 2989	56 572 .95983	−16.6	15.2	−2.87	1.40	M08
8 561 664	HIP 95 876	56 083 .27608	10.0	22.0	6.34	0.90	M11
8 633 854	HD 186 120	56 083 .27596	−16.1	19.3	−26.61	0.12	F05
8 740 371	HD 177 484	56 570 .00722	−5.7	17.1	1.20	0.40	C10
8 752 618	HIP 95 534	56 083 .28250	20.4	19.6	6.90	0.90	G06
8 765 630	HD 186 816	56 083 .27590	−33.0	20.1	−41.00	1.70	F97
8 873 797	2MASS J19073875+4509053	56 570 .00731	−35.2	17.6	−28.60	...	T12
8 894 567	HIP 96 735	56 083.27594	−11.7	18.6	−16.64	0.19	M07
8 894 567	HIP 96 735	56 914.06515	−20.8	16.6	−16.64	0.19	M07
9 161 068	TYC 3556-2027-1	56 083.28093	39.5	19.3	21.20	...	T12
9 161 068	TYC 3556-2027-1	56 914.02662	15.9	19.4	21.20	...	T12
9 206 432	HD 177 723	56 780.30004	−2.4	15.5	−0.85	0.05	D13
9 286 638	HD 185 329	56 083.27587	−25.0	26.6	−27.40	5.00	G99
9 413 057	BD+45 2954	56 083.27586	25.0	37.4	0.89	0.54	Tk12
9 468 475	HIP 96 161	56 083.28094	−2.7	31.6	−23.00	4.50	G06
9 474 021	TYC 3556-3195-1	56 435.28633	−106.2	17.0	−124.00	...	T12
9 528 112	HIP 95 902	56 083.27598	−14.8	55.9	−14.92	1.06	K07
9 532 030	BD+45 2930	56 914.06509	1.2	17.4	−13.50	...	T12
9 532 903	TYC 3556-103-1	56 083.28088	23.0	19.2	6.39	0.46	M14
9 532 903	TYC 3556-103-1	56 435.28637	11.9	17.1	6.39	0.46	M14
9 651 435	HIP 95 980	56 083.27595	−29.9	33.9	−21.70	4.20	G06
9 714 702	HD 184 938	56 083.27591	14.1	17.2	2.80	...	P09
9 716 045	TYC 3556-812-1	56 083.27588	17.7	17.1	5.82	0.13	Me08
9 716 090	TYC 3556-2356-1	56 798.27942	13.6	20.4	6.80	0.43	M14
9 716 090	TYC 3556-2356-1	56 914.06505	−1.4	19.2	6.80	0.43	M14
9 716 220	TYC 3556-1344-1	56 094.21263	−0.7	24.0	4.09	1.07	M14
9 716 431	TYC 3556-590-1	56 083.27588	−1.7	19.9	−8.21	0.54	F08
9 716 667	TYC 3556-914-1	56 914.02659	−4.5	22.3	6.82	1.51	M14
9 775 454	HD 185 115	56 807.27626	−13.2	27.7	−14.70	2.00	W53
9 776 739	TYC 3556-118-1	56 083.27588	11.8	20.0	6.86	0.46	M14
9 776 739	TYC 3556-118-1	56 435.28635	18.9	16.5	6.86	0.46	M14
9 777 108	TYC 3556-1922-1	56 083.27587	−11.4	21.0	−24.81	0.47	F08
9 777 246	TYC 3556-130-1	56 083.27587	2.4	24.8	6.90	0.20	K07
9 777 532	TYC 3556-3228-1	56 435.28633	18.2	18.0	6.58	0.24	M14
9 778 469	HD 186 019	56 083.27585	12.3	26.7	7.00	4.60	F97

Table A.1. continued.

KIC	Name	HJD (−2 400 000)	RV_{LAM} (km s^{-1})	σ_{RV}^{LAM}	RV_{Lit} (km s^{-1})	σ_{RV}^{Lit}	Reference
9 778 469	HD 186 019	56 435.28631	25.5	21.1	7.00	4.60	F97
9 778 469	HD 186 019	56 914.02662	−3.1	25.4	7.00	4.60	F97
9 778 469	HD 186 019	56 914.06509	−0.1	22.3	7.00	4.60	F97
9 779 768	HD 186 356	56 083.27581	14.9	18.9	13.00	3.60	F97
9 782 810	HD 187 119	56 083.27576	−5.0	31.3	22.00	5.60	F97
9 782 810	HD 187 119	56 550.03938	0.9	21.0	22.00	5.60	F97
9 842 399	HD 186 925	56 083.27577	15.2	19.3	4.10	0.60	G06
9 895 798	BD+46 2737	56 083.27588	−38.0	52.8	−23.40	0.24	M14
10 186 608	TYC 3531-194-1	56 780.29668	−5.3	18.1	−11.10	...	T12
10 187 831	BD+47 2698	56 780.29663	−14.4	25.9	−22.70	2.60	C10
10 187 831	BD+47 2698	56 807.23586	−12.9	29.5	−22.70	2.60	C10
10 187 831	BD+47 2698	56 807.27640	−16.2	22.1	−22.70	2.60	C10
10 426 854	BD+47 2960	56 561.00309	−46.3	16.1	−45.60	...	T12
10 604 429	BD+47 2868	55 721.30252	−15.6	17.2	−3.10	1.80	C10
10 960 750	BD+48 2781	56 807.27626	0.9	30.0	−22.00	2.80	C10
10 960 750	BD+48 2781	56 919.01416	−3.3	15.8	−22.00	2.80	C10
11 342 694	TYC 3550-346-1	56 927.99272	−18.0	17.2	−19.90	...	T12
11 444 313	TYC 3549-1225-1	56 919.01428	−23.4	15.7	−17.80	...	T12
11 569 659	TYC 3565-1299-1	56 435.28604	−0.8	16.9	−19.20	...	T12
11 657 684	2MASS J19175551+4946243	56 919.01452	4.6	16.9	14.00	...	T12
11 657 684	2MASS J19175551+4946243	56 930.02147	5.5	18.3	14.00	...	T12

Table A.2. Stars with atmospheric parameters in the literature.

KIC	$T_{\rm eff}^{\rm LAM}$ (K)	err	$T_{\rm eff}^{\rm Lit}$ (K)	err	$\log g^{\rm LAM}$ (dex)	err	$\log g^{\rm Lit}$ (dex)	err	[Fe/H]$^{\rm LAM}$ (dex)	err	[Fe/H]$^{\rm Lit}$ (dex)	err	Reference
1 160 867	4109	95	4000	50	1.92	0.18	...	...	−0.04	0.12	...	...	Ma12
1 161 345	5167	130	5505	112	4.56	0.15	4.56	0.08	0.09	0.13	0.21	0.14	H14
1 430 163	6367	88	6520	60	4.14	0.12	4.22	0.03	−0.22	0.12	−0.11	0.06	B12
1 571 152	6934	158	7065	79	4.07	0.11	4.46	0.38	−0.07	0.12	−0.18	0.10	Tk12
1 726 211	4975	122	4950	70	2.61	0.24	2.36	0.26	−0.24	0.21	−0.66	0.08	B11
2 141 385	3876	105	3760	90	1.61	0.21	...	...	−0.02	0.11	...	...	Ma12
2 162 635	5045	234	5009	92	4.29	0.52	3.76	0.16	0.01	0.15	0.07	0.15	H14
2 165 574	3985	74	3850	60	1.81	0.17	...	...	−0.01	0.12	...	...	Ma12
2 297 384	4404	72	4519	66	2.41	0.23	2.41	...	−0.08	0.12	0.46	0.04	Me13
2 297 825	4430	70	4547	66	2.45	0.20	2.45	...	0.12	0.12	0.44	0.04	Me13
2 302 548	5090	120	5203	102	4.61	0.13	4.60	0.07	0.09	0.14	0.00	0.18	H14
2 424 191	3913	91	3900	60	1.66	0.19	...	...	−0.03	0.12	...	...	Ma12
2 425 631	4589	79	4600	80	2.53	0.17	2.25	0.10	−0.08	0.12	−0.04	0.15	T12
2 435 987	4333	113	4437	71	2.17	0.21	2.24	...	−0.07	0.12	0.33	0.04	Me13
2 581 316	6154	79	6147	120	4.06	0.12	3.90	0.04	0.06	0.12	0.13	0.07	W13
2 837 475	6068	120	6700	60	4.17	0.12	4.16	0.03	−0.68	0.30	−0.02	0.06	B12
2 846 564	3514	80	3520	90	1.02	0.16	...	...	−0.05	0.11	...	...	Ma12
2 998 002	3889	69	3800	70	1.64	0.15	...	...	−0.00	0.11	...	...	Ma12
3 121 983	4067	117	3970	60	1.87	0.20	...	...	−0.06	0.13	...	...	Ma12
3 217 554	8078	650	7830	156	3.92	0.13	3.69	0.15	−0.08	0.13	0.09	0.15	H14
3 218 445	4360	156	4020	50	2.19	0.41	...	...	−0.07	0.13	...	...	Ma12
3 219 256	7078	134	7493	158	4.07	0.14	3.59	0.13	−0.11	0.14	−0.02	0.16	H14
3 221 040	3698	97	3700	80	1.21	0.23	...	...	−0.04	0.12	...	...	Ma12
3 335 176	3149	74	3225	110	0.44	0.12	1.23	1.24	−0.95	0.21	−0.22	0.11	M13
3 424 790	4177	89	4030	50	1.98	0.16	...	...	−0.09	0.12	...	...	Ma12
3 430 868	4759	106	5126	80	2.61	0.13	2.84	0.10	−0.09	0.12	−0.06	0.15	T12
3 438 817	3890	116	3650	70	4.05	1.15	...	...	−0.17	0.16	0.33	0.12	Ma12
3 453 494	7720	160	7737	57	3.86	0.15	3.71	0.22	−0.13	0.12	−0.95	0.00	Tk12
3 456 181	6259	112	6270	60	4.13	0.12	3.93	0.03	−0.19	0.12	−0.19	0.06	B12
3 640 905	4527	106	4991	75	2.72	0.17	3.62	0.01	0.08	0.12	0.28	0.10	H14
3 656 476	5576	156	5710	60	4.21	0.28	4.23	0.03	0.12	0.15	0.34	0.06	B12
3 748 585	4545	107	4615	80	2.61	0.13	2.58	0.10	−0.00	0.12	0.25	0.15	T12
3 748 691	4574	106	4750	80	2.57	0.14	2.45	0.10	−0.01	0.12	0.10	0.15	T12
3 756 031	18 767	570	15 980	310	3.76	0.11	3.75	0.06	−0.00	0.10	−0.57	0.08	L11
3 836 453	5038	108	4954	99	4.61	0.12	4.59	0.15	0.01	0.17	−0.06	0.15	H14
3 839 930	16 385	1215	16 500	0	3.78	0.11	4.20	0.00	0.01	0.12	...	...	Ba11
3 859 079	4418	208	4744	94	4.61	0.12	4.61	0.05	−0.11	0.13	0.10	0.16	H14
3 860 139	4425	71	4550	90	2.35	0.17	2.23	0.25	0.03	0.12	0.25	0.13	B11
3 865 742	20 315	735	19 500	0	3.78	0.12	3.70	0.00	−0.03	0.10	...	...	Ba11
3 942 670	5842	82	6010	124	4.23	0.13	4.28	0.13	0.03	0.13	0.08	0.14	H14
3 955 590	4439	63	4645	80	2.50	0.16	2.23	0.10	0.11	0.13	−0.16	0.15	T12
3 964 632	3931	75	3950	70	1.74	0.17	...	...	0.00	0.11	...	...	Ma12
4 060 815	4917	104	5055	75	2.98	0.29	...	...	−0.04	0.13	−0.07	0.10	H14
4 070 746	4952	109	5150	80	2.82	0.25	3.23	0.10	−0.23	0.16	−0.17	0.15	T12
4 141 376	6161	95	6134	91	4.18	0.12	...	...	−0.32	0.14	−0.24	0.10	H13
4 143 755	5791	93	5622	106	4.24	0.12	...	...	−0.45	0.13	−0.40	0.11	H13
4 147 309	3428	105	3520	90	0.78	0.25	...	...	−0.07	0.11	...	...	Ma12
4 161 741	4846	81	4859	56	2.67	0.13	2.79	0.15	−0.03	0.12	−0.16	0.10	M08
4 177 025	4481	121	4390	90	2.50	0.19	1.85	0.29	−0.11	0.12	−0.25	0.11	B11
4 180 280	5029	118	4911	101	4.59	0.13	4.57	0.05	0.04	0.14	0.26	0.14	H14
4 242 575	6167	118	6397	0	4.12	0.17	...	...	−0.08	0.19	0.25	...	N04
4 278 221	5910	93	5977	121	4.21	0.14	4.47	0.16	0.07	0.12	0.21	0.17	H14
4 283 484	5000	144	5030	80	2.55	0.27	2.40	0.10	−0.58	0.18	−0.78	0.15	T12
4 346 201	6172	78	6154	81	4.13	0.12	3.98	0.12	−0.31	0.12	−0.25	0.11	M13
4 385 594	3925	90	3870	70	1.72	0.18	...	...	−0.05	0.12	...	...	Ma12

Notes. B11 = Bruntt et al. (2011); B12 = Bruntt et al. (2012); Ba11 = Balona et al. (2011); Ba13 = Batalha et al. (2013); Bu12 = Buchhave et al. (2012); C10 = Catanzaro et al. (2010); C11 = Catanzaro et al. (2011); Ca11 = Casagrande et al. (2011); F11 = Frasca et al. (2011); F12 = Fröhlich et al. (2012); H13 = Huber et al. (2013); H14 = Huber et al. (2014) spectroscopic data only; H98 = Hauck & Mermilliod (1998); L11 = Lehmann et al. (2011); M07 = Molenda-Żakowicz et al. (2007); M08 = Molenda-Żakowicz et al. (2008); M13 = Molenda-Żakowicz et al. (2013); M14 = Molenda-Żakowicz et al. (2014); Ma12 = Mann et al. (2012); Ma14 = Marcy et al. (2014); Me13 = Meszaros et al. (2013); N04 = Nordström et al. (2004); N14 = Niemczura et al. (2015); P09 = Pakhomov et al. (2009); P13 = Petigura et al. (2013); T12 = Thygesen et al. (2012); Tk12 = Tkachenko et al. (2012); To12 = Torres et al. (2012); U11 = Uytterhoeven et al. (2011b); W13 = Wang et al. (2013).

Table A.2. continued.

KIC	$T_{\rm eff}^{\rm LAM}$ (K)	err	$T_{\rm eff}^{\rm Lit}$ (K)	err	$\log g^{\rm LAM}$ (dex)	err	$\log g^{\rm Lit}$ (dex)	err	[Fe/H]$^{\rm LAM}$ (dex)	err	[Fe/H]$^{\rm Lit}$ (dex)	err	Reference
4 476 423	4584	123	4553	97	2.50	0.21	...	...	−0.01	0.12	0.42	0.16	H14
4 478 168	6047	136	6157	129	4.18	0.12	4.45	0.12	−0.17	0.14	−0.12	0.16	H14
4 548 011	5942	105	5990	119	4.17	0.15	4.30	0.15	0.08	0.13	0.04	0.15	H14
4 551 429	3649	171	3580	70	1.49	0.82	...	...	−0.11	0.14	0.18	0.12	Ma12
4 563 268	5806	130	6077	135	4.14	0.15	4.44	0.17	0.04	0.12	0.21	0.17	H14
4 581 434	9836	409	10 200	200	3.85	0.13	4.20	0.20	−0.19	0.15	...	...	C10
4 586 119	6257	66	6296	60	4.06	0.12	4.02	0.03	0.01	0.11	−0.17	0.06	B12
4 644 604	5340	223	5741	113	3.96	0.52	4.34	0.14	−0.82	0.41	−0.38	0.16	H14
4 655 612	3919	209	3730	60	2.94	1.08	...	...	−0.19	0.18	−0.36	0.14	Ma12
4 659 706	4429	65	4450	80	2.53	0.17	2.46	0.10	0.17	0.12	0.62	0.15	T12
4 678 401	3662	87	3600	70	1.14	0.21	...	...	−0.03	0.12	...	...	Ma12
4 726 192	4031	141	3770	60	4.63	0.25	...	...	−0.24	0.13	−0.09	0.16	Ma12
4 742 414	5784	86	5868	125	4.17	0.16	4.17	0.13	−0.23	0.17	0.10	0.14	H14
4 827 723	5254	199	5441	106	4.30	0.39	4.50	0.12	0.05	0.12	0.04	0.16	H14
4 832 837	4213	101	3941	73	4.61	0.18	4.71	0.10	−0.18	0.12	−0.03	0.14	H14
4 857 678	6464	80	6668	0	4.13	0.11	...	...	−0.24	0.13	−0.10	...	N04
4 860 890	3798	158	3730	80	1.56	0.31	...	...	−0.21	0.15	...	...	Ma12
4 914 423	5815	77	5845	88	4.22	0.13	4.27	0.00	0.11	0.13	0.07	0.11	P13
4 914 566	6016	155	5974	0	4.12	0.13	4.22	0.00	−0.39	0.17	...	...	P13
4 914 923	5765	93	5905	60	4.22	0.21	4.21	0.03	0.11	0.13	0.17	0.06	B12
4 927 048	3889	70	3800	70	1.65	0.15	...	...	0.00	0.11	...	...	Ma12
4 931 363	7041	175	7045	106	4.02	0.15	4.07	0.12	−0.05	0.14	−0.05	0.11	M13
4 937 056	4848	119	4803	83	2.56	0.18	2.82	...	−0.14	0.15	0.02	0.05	Me13
4 937 576	4558	88	4607	82	2.62	0.15	2.45	...	−0.01	0.12	0.04	0.05	Me13
4 947 556	5049	181	5122	96	4.13	0.42	4.66	0.03	0.07	0.12	0.26	0.06	W13
5 009 743	5875	152	5934	117	4.15	0.13	4.35	0.13	−0.62	0.23	−0.30	0.16	H14
5 023 732	4515	76	4564	82	2.55	0.17	2.37	...	−0.02	0.11	0.04	0.05	Me13
5 024 240	4946	115	4888	88	2.77	0.25	2.98	...	−0.11	0.16	−0.09	0.06	Me13
5 024 851	4093	94	4130	80	1.89	0.18	1.64	...	−0.03	0.13	0.09	0.05	Me13
5 024 967	4714	74	4757	81	2.60	0.13	2.67	...	−0.05	0.11	0.07	0.05	Me13
5 032 507	3960	94	3700	80	1.73	0.16	...	...	−0.03	0.12	...	...	Ma12
5 039 228	6422	80	6543	130	4.11	0.11	4.39	0.15	0.02	0.11	0.25	0.15	H14
5 079 307	3576	113	3860	80	1.02	0.24	...	...	−0.03	0.12	...	...	Ma12
5 080 290	5308	280	5157	153	3.25	0.53	3.60	0.30	−0.12	0.20	−0.06	0.12	M13
5 088 536	5909	91	5884	75	4.16	0.13	...	...	−0.22	0.15	−0.22	0.10	H13
5 093 678	3856	136	3880	70	1.64	0.20	...	...	−0.19	0.13	...	...	Ma12
5 094 751	5883	90	5952	75	4.14	0.14	4.21	0.04	−0.02	0.17	−0.08	0.10	Ma14
5 096 590	5771	108	5623	0	4.26	0.19	4.63	0.00	0.08	0.13	...	...	P13
5 111 940	4837	98	4688	82	2.57	0.15	2.65	0.00	−0.16	0.13	0.06	0.05	Me13
5 112 072	4909	116	4869	82	2.66	0.21	2.97	0.00	−0.22	0.15	0.04	0.05	Me13
5 112 481	4193	108	4221	82	1.93	0.20	1.75	0.00	−0.04	0.12	0.05	0.05	Me13
5 112 730	4654	84	4748	80	2.58	0.14	2.64	0.00	0.02	0.10	0.09	0.05	Me13
5 112 786	4439	129	4207	57	2.30	0.24	1.99	0.11	−0.04	0.13	−0.17	0.10	M13
5 112 950	4604	89	4726	80	2.56	0.15	2.63	0.00	−0.02	0.12	0.09	0.05	Me13
5 112 974	4706	79	4742	82	2.62	0.12	2.60	0.00	−0.01	0.11	0.04	0.05	Me13
5 113 041	4553	82	4641	84	2.55	0.16	2.46	0.00	−0.02	0.11	0.01	0.05	Me13
5 113 061	4125	96	4196	79	1.91	0.17	1.75	0.00	−0.03	0.12	0.11	0.05	Me13
5 113 910	4485	76	4510	80	2.39	0.19	1.75	0.10	−0.14	0.12	−0.31	0.15	T12
5 121 511	5164	152	5275	121	4.02	0.41	4.43	0.10	0.07	0.11	0.06	0.16	H14
5 129 367	3712	109	3640	60	1.31	0.25	...	...	−0.06	0.11	...	...	Ma12
5 130 305	10 389	798	10 670	190	3.93	0.13	3.86	0.07	−0.15	0.12	−0.07	0.11	L11
5 199 859	3485	85	3722	112	0.99	0.17	1.63	0.30	−0.06	0.11	−0.07	0.11	M13
5 206 997	4529	280	4365	184	4.50	0.33	4.57	0.15	−0.16	0.16	−0.15	0.15	M07
5 284 127	4565	104	4660	80	2.61	0.16	2.46	0.10	0.03	0.12	0.45	0.15	T12
5 296 877	6546	145	6500	200	4.15	0.11	3.80	0.30	−0.32	0.16	...	...	C11
5 341 903	4420	80	4080	60	2.28	0.20	...	...	0.03	0.15	...	...	Ma12
5 383 248	5694	97	5690	73	4.26	0.15	4.42	0.08	−0.02	0.17	0.04	0.07	Ma14
5 395 743	4190	140	3930	60	1.86	0.26	...	...	−0.14	0.13	...	...	Ma12
5 437 945	6079	116	6079	195	4.10	0.13	3.96	0.30	−0.02	0.14	−0.39	0.50	W13
5 442 047	4150	87	4072	66	1.90	0.17	1.75	0.10	−0.04	0.12	−0.19	0.06	M08
5 446 068	5996	170	5980	120	4.07	0.15	3.58	0.28	0.01	0.17	0.24	0.10	U11
5 446 285	5328	206	5581	111	4.11	0.29	4.54	0.15	0.11	0.12	0.39	0.15	H14
5 476 864	6701	188	6550	131	4.07	0.12	3.72	0.15	−0.04	0.13	−0.18	0.15	H14
5 511 081	5937	100	5923	77	4.05	0.13	...	...	0.02	0.13	−0.07	0.10	H13
5 511 423	4867	96	4320	80	2.62	0.19	1.33	0.10	−0.51	0.14	−0.96	0.15	T12

Table A.2. continued.

KIC	$T_{\rm eff}^{\rm LAM}$ (K)	err	$T_{\rm eff}^{\rm Lit}$ (K)	err	$\log g^{\rm LAM}$ (dex)	err	$\log g^{\rm Lit}$ (dex)	err	$[{\rm Fe/H}]^{\rm LAM}$ (dex)	err	$[{\rm Fe/H}]^{\rm Lit}$ (dex)	err	Reference
5 512 589	5833	75	5750	60	4.15	0.14	4.06	0.03	0.10	0.12	0.06	0.06	B12
5 513 861	6367	98	6528	144	4.15	0.11	4.38	0.16	−0.29	0.15	−0.16	0.18	H14
5 514 383	6177	77	6184	81	4.12	0.11	...	...	0.04	0.12	0.12	0.10	H13
5 524 720	4349	106	4350	80	2.29	0.23	2.23	0.10	0.01	0.13	0.38	0.15	T12
5 561 278	6104	123	6081	75	4.07	0.13	...	...	−0.05	0.13	−0.03	0.10	H13
5 600 727	3745	85	3680	80	1.46	0.21	...	...	−0.04	0.11	...	...	Ma12
5 612 549	4868	72	4800	80	2.52	0.12	2.38	0.10	−0.27	0.12	−0.33	0.15	T12
5 613 330	6240	98	6079	121	4.08	0.12	4.20	0.15	−0.01	0.14	0.13	0.15	H14
5 648 449	3559	80	3600	70	1.01	0.17	...	...	−0.06	0.11	...	...	Ma12
5 683 912	3147	74	3000	90	0.39	0.14	...	...	−0.96	0.19	...	...	Ma12
5 695 396	5772	80	5809	116	4.22	0.14	4.56	0.15	0.13	0.13	0.22	0.15	H14
5 701 829	4886	129	4914	56	2.82	0.27	3.18	0.12	−0.23	0.16	−0.13	0.11	M13
5 708 328	3936	84	3800	60	1.74	0.16	...	...	−0.02	0.12	...	...	Ma12
5 709 564	4745	73	4775	70	2.57	0.12	2.46	0.25	−0.18	0.13	−0.22	0.08	B11
5 732 026	4118	103	3860	70	1.80	0.19	...	...	−0.08	0.11	...	...	Ma12
5 735 762	5335	180	5315	106	4.16	0.35	4.64	0.15	0.05	0.13	0.31	0.15	H14
5 785 707	8174	328	7965	70	3.93	0.11	3.37	0.15	−0.19	0.13	−0.56	0.11	Tk12
5 786 771	10 295	782	10 700	500	3.91	0.12	4.20	0.20	−0.18	0.14	...	...	C10
5 792 581	5443	295	4980	80	3.60	0.50	2.82	0.10	0.04	0.15	−0.22	0.15	T12
5 810 113	7044	142	6480	129	3.78	0.17	3.60	0.15	0.15	0.13	0.24	0.15	H14
5 858 889	3821	81	3810	70	1.55	0.16	...	...	−0.04	0.11	...	...	Ma12
5 859 492	4485	101	4800	80	2.45	0.21	2.49	0.10	0.15	0.12	0.19	0.15	T12
5 866 724	6196	89	6172	50	4.03	0.13	4.39	0.10	0.03	0.12	0.12	0.08	Bu12
5 905 446	3717	72	3650	70	1.38	0.21	...	...	−0.04	0.11	...	...	Ma12
5 959 719	5076	183	5165	103	3.63	0.53	4.57	0.15	−0.06	0.15	−0.12	0.15	H14
5 964 115	3769	109	3750	80	1.42	0.22	...	...	−0.09	0.12	...	...	Ma12
5 965 837	7079	172	6975	200	3.71	0.14	4.00	0.40	0.24	0.13	...	...	C11
5 966 322	5637	98	5598	110	4.34	0.14	4.32	0.14	−0.27	0.16	−0.12	0.18	H14
5 977 048	4093	103	3860	70	1.85	0.20	...	...	−0.05	0.12	...	...	Ma12
6 127 362	3659	106	3670	70	1.18	0.23	...	...	−0.04	0.12	...	...	Ma12
6 129 655	4043	109	3920	50	1.79	0.17	...	...	−0.03	0.12	...	...	Ma12
6 185 476	4060	139	3745	80	4.62	0.12	4.78	0.15	−0.23	0.13	−0.02	0.15	H14
6 196 457	5860	80	5883	50	4.08	0.14	4.10	0.10	0.13	0.12	0.10	0.08	Bu12
6 268 648	6277	97	6044	117	4.16	0.11	...	...	−0.27	0.14	−0.24	0.11	H13
6 271 813	4426	115	4070	50	2.15	0.21	...	...	−0.46	0.13	...	...	Ma12
6 285 677	5913	91	5849	64	4.18	0.13	4.32	0.12	0.07	0.12	0.06	0.12	M13
6 289 468	8278	99	8107	70	3.85	0.12	3.30	0.06	−0.20	0.10	−0.48	0.11	Tk12
6 291 837	6100	139	6165	0	4.20	0.12	4.38	0.00	−0.41	0.16	0.01	0.08	P13
6 301 745	6941	111	6735	135	4.09	0.10	4.01	0.16	−0.14	0.12	−0.44	0.14	H14
6 360 007	4286	147	3930	60	2.07	0.26	...	...	−0.07	0.14	...	...	Ma12
6 365 156	5814	365	5850	122	4.08	0.18	4.28	0.13	−0.32	0.20	−0.04	0.16	H14
6 509 175	7312	216	7520	150	3.90	0.13	3.30	0.15	−0.02	0.12	−0.24	0.15	H14
6 523 351	5630	107	5489	0	4.23	0.21	4.15	0.00	0.10	0.14	...	...	P13
6 541 920	5771	100	5680	100	4.21	0.15	4.30	0.20	0.12	0.16	0.00	0.10	Bu12
6 579 998	5280	312	5070	80	3.43	0.58	2.45	0.10	−0.47	0.16	−0.69	0.15	T12
6 590 668	4873	151	4463	58	2.68	0.22	2.02	0.12	−0.13	0.17	−0.22	0.10	M13
6 616 218	5202	162	5501	110	4.04	0.35	4.66	0.15	0.08	0.11	0.38	0.15	H14
6 616 432	6443	68	6247	164	4.13	0.11	4.01	0.08	−0.20	0.14	−0.33	0.11	M08
6 678 383	5874	105	5724	114	4.22	0.13	4.14	0.15	−0.42	0.16	−0.57	0.15	H14
6 680 734	4823	100	4580	80	2.65	0.20	2.17	0.10	−0.20	0.16	−0.38	0.15	T12
6 695 442	3516	65	3630	70	1.02	0.17	...	...	−0.06	0.11	...	...	Ma12
6 696 436	4700	100	4630	80	2.57	0.17	2.33	0.10	−0.16	0.12	−0.26	0.15	T12
6 707 835	5668	105	5789	115	4.27	0.18	4.65	0.15	0.13	0.13	0.35	0.15	H14
6 766 118	4904	119	4892	58	2.89	0.21	2.73	0.10	−0.02	0.15	0.05	0.10	M13
6 837 256	4941	123	4850	80	2.68	0.26	2.48	0.10	−0.46	0.16	−0.65	0.15	T12
6 843 652	4222	174	3860	70	1.90	0.29	...	...	−0.29	0.14	...	...	Ma12
6 848 529	19 632	766	19 300	1000	3.78	0.11	3.80	0.20	−0.03	0.10	...	...	C10
6 850 504	5676	104	5563	49	4.22	0.15	4.52	0.10	0.08	0.16	0.03	0.08	Bu12
6 922 244	6242	81	6251	75	4.07	0.13	4.19	0.04	−0.15	0.13	0.05	0.09	To12
6 922 710	5869	84	5929	118	4.16	0.14	4.40	0.15	−0.05	0.18	−0.05	0.15	H14

Table A.2. continued.

KIC	$T_{\rm eff}^{\rm LAM}$ (K)	err	$T_{\rm eff}^{\rm Lit}$ (K)	err	$\log g^{\rm LAM}$ (dex)	err	$\log g^{\rm Lit}$ (dex)	err	$[{\rm Fe/H}]^{\rm LAM}$ (dex)	err	$[{\rm Fe/H}]^{\rm Lit}$ (dex)	err	Reference
6 956 014	3981	75	4029	80	1.79	0.15	1.77	0.15	−0.05	0.12	−0.16	0.15	H14
6 975 129	6046	128	6197	123	4.11	0.11	4.55	0.15	−0.03	0.14	0.20	0.15	H14
6 976 475	5742	91	5749	151	4.24	0.13	4.22	0.26	−0.37	0.13	−0.24	0.21	M07
7 048 122	4142	88	4030	50	1.85	0.21	...	...	0.01	0.11	...	...	Ma12
7 050 989	6184	66	6158	123	4.05	0.13	4.35	0.15	0.02	0.11	0.12	0.15	H14
7 051 180	5445	231	5404	50	3.94	0.36	4.02	0.10	−0.12	0.17	0.10	0.08	Bu12
7 106 205	7049	166	6900	138	3.89	0.18	3.73	0.15	0.06	0.15	0.30	0.15	H14
7 115 785	5694	113	5515	110	4.28	0.18	4.34	0.15	0.11	0.14	0.01	0.15	H14
7 122 746	8046	230	7740	154	3.92	0.12	4.00	0.15	−0.16	0.11	0.09	0.15	H14
7 185 134	3834	134	3640	60	1.49	0.30	...	...	−0.19	0.12	...	...	Ma12
7 199 397	6053	158	5824	50	4.03	0.14	3.70	0.10	0.07	0.14	−0.22	0.08	Bu12
7 206 837	6179	95	6304	60	4.05	0.12	4.17	0.03	0.10	0.11	0.14	0.06	B12
7 211 221	5757	84	5634	112	4.32	0.14	4.44	0.15	0.05	0.14	−0.21	0.15	H14
7 215 603	6139	73	6173	93	4.06	0.12	...	...	0.08	0.11	0.17	0.10	H13
7 255 336	6296	108	6211	124	4.13	0.11	4.19	0.15	−0.26	0.14	−0.24	0.15	H14
7 277 317	4770	136	4883	75	3.03	0.39	...	...	0.07	0.12	0.16	0.10	H13
7 282 890	6387	84	6384	60	4.07	0.12	3.88	0.03	−0.03	0.13	0.02	0.06	B12
7 295 235	5382	122	5543	110	4.46	0.23	4.59	0.15	0.07	0.12	0.06	0.15	H14
7 345 435	4392	69	4150	40	2.10	0.18	...	...	−0.12	0.11	...	...	Ma12
7 354 482	3979	188	3840	60	1.76	0.25	...	...	−0.11	0.14	...	...	Ma12
7 364 176	5759	95	5704	114	4.23	0.13	4.34	0.15	−0.41	0.14	−0.44	0.15	H14
7 374 855	4596	90	4599	48	2.60	0.14	2.27	0.12	0.09	0.12	−0.07	0.05	M08
7 449 136	6046	119	6099	75	4.04	0.13	...	...	0.05	0.11	0.04	0.10	H13
7 451 886	3848	84	3800	80	1.59	0.15	...	...	−0.03	0.11	...	...	Ma12
7 505 113	3566	110	3330	90	1.07	0.24	...	...	−0.10	0.12	...	...	Ma12
7 515 212	5847	73	5913	118	4.15	0.14	4.37	0.15	0.06	0.15	0.32	0.15	H14
7 534 293	3910	84	3800	60	1.70	0.17	...	...	0.00	0.11	...	...	Ma12
7 582 689	5921	168	6022	0	4.16	0.15	4.04	0.00	−0.16	0.17	...	...	P13
7 599 132	11 251	860	11 090	120	3.99	0.12	4.08	0.06	−0.03	0.11	0.06	0.10	L11
7 601 633	6078	136	5997	119	4.02	0.13	3.90	0.15	−0.05	0.17	0.23	0.15	H14
7 603 200	4128	212	3841	80	4.48	0.49	4.76	0.15	−0.23	0.16	−0.18	0.15	H14
7 619 236	5560	238	5592	111	4.27	0.27	4.23	0.15	0.12	0.13	0.34	0.15	H14
7 630 229	5804	89	5887	117	4.15	0.14	4.38	0.15	0.07	0.14	0.15	0.15	H14
7 668 663	5785	91	5725	114	4.18	0.14	4.33	0.15	0.06	0.14	−0.06	0.15	H14
7 680 114	5816	72	5855	60	4.13	0.14	4.18	0.03	0.09	0.13	0.11	0.06	B12
7 693 833	4947	155	4880	80	2.08	0.37	2.46	0.10	-2.22	0.22	-2.23	0.15	T12
7 729 057	4266	109	3990	50	2.14	0.19	...	...	−0.01	0.12	...	...	Ma12
7 748 238	7235	177	7260	145	3.91	0.13	4.06	0.15	0.05	0.14	−0.14	0.15	H14
7 765 135	5866	94	5835	95	4.19	0.14	4.34	0.12	−0.04	0.18	0.04	0.05	F12
7 768 995	3959	72	3800	60	1.77	0.15	...	...	−0.02	0.12	...	...	Ma12
7 799 349	4893	121	5115	60	2.97	0.26	3.67	0.03	0.09	0.12	0.41	0.06	B12
7 800 289	6433	84	6354	60	4.09	0.11	3.71	0.03	−0.21	0.12	−0.23	0.06	B12
7 812 552	5207	265	5070	80	3.70	0.51	3.26	0.10	−0.47	0.17	−0.59	0.15	T12
7 826 659	4847	161	4675	188	3.62	0.47	4.58	0.30	−0.03	0.16	0.40	0.09	W13
7 887 791	5677	106	5548	110	4.28	0.16	4.39	0.15	−0.02	0.17	−0.05	0.15	H14
7 918 217	3832	132	3630	70	1.45	0.29	...	...	−0.18	0.14	...	...	Ma12
7 966 601	3703	74	3630	60	1.36	0.18	...	...	−0.05	0.11	...	...	Ma12
7 985 370	5842	74	5815	95	4.22	0.12	4.24	0.12	0.05	0.13	−0.05	0.10	F12
7 985 592	3776	121	3500	90	1.38	0.23	...	...	−0.10	0.13	...	...	Ma12
8 008 067	5717	120	5615	112	4.21	0.18	4.29	0.15	0.12	0.14	0.40	0.15	H14
8 024 865	3802	119	3600	80	1.36	0.25	...	...	−0.14	0.13	...	...	Ma12
8 030 148	5783	83	5723	114	4.24	0.12	4.14	0.15	−0.26	0.15	−0.16	0.15	H14
8 073 705	6193	109	6086	121	4.09	0.12	4.36	0.15	−0.15	0.14	−0.14	0.15	H14
8 081 187	6114	170	6030	0	4.11	0.12	4.55	0.00	−0.19	0.14	...	...	P13
8 087 269	14 812	1003	14 500	0	3.74	0.11	3.90	0.00	0.07	0.11	...	...	Ba11
8 087 812	6155	128	5984	119	4.10	0.13	4.17	0.15	−0.26	0.15	−0.33	0.15	H14
8 091 051	4456	212	4080	60	2.42	0.25	...	...	−0.01	0.15	...	...	Ma12
8 158 779	3868	117	3700	90	1.62	0.22	...	...	−0.16	0.13	...	...	Ma12
8 161 798	12 325	578	12 300	0	4.06	0.12	4.00	0.00	0.19	0.18	...	...	Ba11
8 179 536	6344	90	6344	60	4.15	0.11	4.27	0.03	−0.01	0.12	0.01	0.06	B12

Table A.2. continued.

KIC	$T_{\rm eff}^{\rm LAM}$ (K)	err	$T_{\rm eff}^{\rm Lit}$ (K)	err	$\log g^{\rm LAM}$ (dex)	err	$\log g^{\rm Lit}$ (dex)	err	$[{\rm Fe/H}]^{\rm LAM}$ (dex)	err	$[{\rm Fe/H}]^{\rm Lit}$ (dex)	err	Reference
8 191 672	6365	95	6297	60	4.06	0.11	3.96	0.10	−0.04	0.13	0.04	0.06	Bu12
8 219 268	4535	75	4605	97	2.58	0.19	...	...	0.09	0.12	0.29	0.16	H13
8 223 568	6559	135	6740	134	4.13	0.11	4.38	0.15	−0.22	0.13	0.02	0.15	H14
8 226 149	4346	170	4260	40	2.23	0.27	...	...	−0.05	0.14	...	...	Ma12
8 228 742	6129	151	6042	60	4.08	0.14	4.02	0.03	−0.13	0.16	−0.14	0.06	B12
8 242 434	4851	170	4691	93	4.60	0.12	4.63	0.15	−0.01	0.15	0.04	0.15	H14
8 264 698	7607	283	7500	150	3.92	0.12	3.90	0.15	−0.07	0.13	−0.07	0.15	H14
8 278 371	5812	68	5731	114	4.14	0.14	4.33	0.15	0.13	0.12	0.02	0.15	H14
8 323 753	6070	133	5817	0	4.08	0.13	4.23	0.00	0.02	0.14	...	...	P13
8 346 342	6254	71	6141	94	4.01	0.12	3.93	0.11	−0.05	0.12	−0.05	0.12	M13
8 349 582	5750	88	5659	50	4.24	0.13	4.10	0.10	0.11	0.13	0.29	0.08	Bu12
8 359 498	5586	173	5716	114	4.16	0.21	4.63	0.15	0.21	0.13	0.44	0.15	H14
8 381 949	19 951	1257	24 500	0	3.73	0.14	4.30	0.00	−0.01	0.10	...	...	Ba11
8 389 948	10 568	358	10 240	280	3.89	0.12	3.86	0.11	−0.16	0.14	0.10	0.12	L11
8 417 203	3929	97	3770	70	1.78	0.25	...	...	−0.18	0.13	...	...	Ma12
8 427 166	3787	102	3690	90	1.46	0.26	...	...	−0.15	0.13	...	...	Ma12
8 429 280	4933	171	5055	135	4.09	0.47	4.41	0.25	0.07	0.12	−0.02	0.10	F11
8 435 766	5148	137	5089	101	4.61	0.12	4.60	0.15	0.07	0.13	−0.14	0.15	H14
8 445 780	4475	152	4250	50	2.46	0.29	...	...	0.15	0.16	...	...	Ma12
8 480 285	5964	132	5959	119	4.19	0.12	4.36	0.15	−0.44	0.16	−0.26	0.15	H14
8 488 717	10 332	795	11 000	0	3.92	0.12	4.00	0.00	−0.11	0.13	...	...	Ba11
8 491 147	4997	133	5050	80	2.59	0.24	2.49	0.10	−0.31	0.25	−0.51	0.15	T12
8 493 586	3636	123	3610	80	1.28	0.26	...	...	−0.16	0.13	...	...	Ma12
8 493 969	4765	93	4830	80	2.58	0.18	2.97	0.10	−0.28	0.14	−0.20	0.15	T12
8 494 142	6100	123	6144	106	4.06	0.13	...	...	−0.05	0.13	0.13	0.10	H13
8 494 617	5896	116	5904	118	4.08	0.15	4.36	0.15	0.01	0.14	−0.09	0.15	H14
8 504 443	6098	122	6333	83	4.10	0.14	...	...	−0.26	0.15	...	...	Ca11
8 510 314	4326	135	3990	50	2.11	0.26	...	...	−0.10	0.16	...	...	Ma12
8 539 201	5099	203	4947	155	2.58	0.26	2.50	0.16	−0.53	0.18	−0.57	0.10	M08
8 554 498	5837	68	5753	75	4.12	0.14	...	...	0.09	0.12	0.05	0.10	H13
8 559 644	5815	70	5907	118	4.15	0.13	4.36	0.15	0.16	0.11	0.23	0.15	H14
8 560 804	5902	84	5878	0	4.05	0.13	4.44	0.00	0.11	0.11	...	...	P13
8 561 221	5230	208	5245	60	3.50	0.41	3.61	0.03	−0.13	0.17	−0.06	0.06	B12
8 561 664	6212	248	6276	80	4.15	0.13	...	...	−0.55	0.28	...	...	Ca11
8 582 121	3865	108	3630	70	1.56	0.25	...	...	−0.12	0.14	...	...	Ma12
8 583 770	10 651	481	9690	200	3.98	0.12	3.39	0.07	−0.06	0.13	0.18	0.09	L11
8 607 720	4964	106	5066	75	2.87	0.30	...	...	−0.25	0.15	−0.33	0.10	H13
8 611 832	5768	91	5576	111	4.20	0.14	4.37	0.15	−0.38	0.15	−0.39	0.15	H14
8 623 953	7813	104	7726	50	3.87	0.11	3.43	0.18	−0.11	0.10	−0.35	0.08	Tk12
8 628 758	5719	94	5773	115	4.28	0.16	4.40	0.15	−0.02	0.16	−0.04	0.15	H14
8 686 097	5869	131	5833	116	4.25	0.13	4.20	0.15	−0.20	0.18	−0.27	0.15	H14
8 700 771	5836	74	5665	113	4.24	0.13	3.86	0.15	−0.29	0.13	−0.39	0.15	H14
8 701 255	3725	77	3760	70	1.44	0.14	...	...	−0.12	0.14	...	...	Ma12
8 702 606	5599	183	5540	60	3.99	0.42	3.76	0.03	−0.04	0.19	−0.09	0.06	B12
8 711 794	5753	87	5575	111	4.23	0.13	4.14	0.15	−0.35	0.14	−0.44	0.15	H14
8 714 886	17 487	903	19 000	380	3.79	0.11	4.30	0.15	−0.03	0.10	−0.10	0.15	H14
8 738 809	6043	88	6090	60	4.05	0.11	3.90	0.03	0.08	0.11	0.11	0.06	B12
8 738 899	3848	140	3780	70	1.66	0.21	...	...	−0.22	0.14	...	...	Ma12
8 740 371	9246	243	9100	400	3.82	0.13	3.70	0.20	−0.23	0.13	...	...	C10
8 750 029	7289	216	7340	146	3.90	0.14	3.70	0.15	0.03	0.14	0.04	0.15	H14
8 750 712	4016	92	3900	60	1.83	0.14	...	...	−0.07	0.11	...	...	Ma12
8 753 657	5599	130	5538	75	4.39	0.17	4.41	0.02	0.16	0.13	0.18	0.07	Ma14
8 760 414	5991	120	5787	60	4.18	0.11	4.33	0.03	−0.72	0.15	-1.14	0.06	B12
8 804 455	5721	82	5714	114	4.34	0.15	4.38	0.15	0.12	0.13	0.04	0.15	H14
8 816 903	6952	143	7063	122	4.08	0.11	4.12	0.10	−0.12	0.13	−0.05	0.10	M13
8 822 366	6133	103	6034	92	4.11	0.12	...	...	−0.19	0.19	−0.14	0.10	H13
8 866 102	6258	71	6195	113	4.13	0.11	3.95	0.10	−0.06	0.12	−0.16	0.11	M13
8 873 797	4643	111	4500	80	2.51	0.19	2.41	0.10	−0.13	0.14	0.32	0.15	T12
8 894 567	5133	80	5131	123	4.61	0.12	4.37	0.11	0.01	0.16	−0.10	0.11	M07
8 938 364	5753	71	5630	60	4.26	0.12	4.16	0.03	0.05	0.13	−0.20	0.06	B12

Table A.2. continued.

KIC	$T_{\rm eff}^{\rm LAM}$ (K)	err	$T_{\rm eff}^{\rm Lit}$ (K)	err	$\log g^{\rm LAM}$ (dex)	err	$\log g^{\rm Lit}$ (dex)	err	[Fe/H]$^{\rm LAM}$ (dex)	err	[Fe/H]$^{\rm Lit}$ (dex)	err	Reference
8 972 058	5962	114	5978	119	4.19	0.13	4.38	0.15	−0.06	0.18	−0.10	0.15	H14
9 002 278	5164	195	4772	95	4.22	0.40	4.28	0.15	−0.33	0.18	−0.52	0.15	H14
9 006 186	5231	131	5403	108	4.53	0.15	4.53	0.15	0.11	0.12	0.19	0.15	H14
9 015 738	5871	78	6037	120	4.19	0.13	4.53	0.15	0.05	0.13	0.21	0.15	H14
9 025 370	5737	92	5720	77	4.35	0.15	4.30	0.12	0.08	0.14	−0.18	0.15	M13
9 032 900	5976	94	6043	120	4.05	0.11	4.07	0.15	0.12	0.11	0.34	0.15	H14
9 051 345	3501	134	3350	110	0.89	0.37	...	...	−0.11	0.14	...	...	Ma12
9 071 386	6199	77	6359	127	4.06	0.12	4.22	0.15	0.07	0.11	0.19	0.15	H14
9 086 251	6111	109	6044	120	4.12	0.12	4.22	0.15	0.07	0.12	0.11	0.15	H14
9 098 294	5852	83	5840	60	4.24	0.12	4.30	0.03	0.03	0.13	−0.13	0.06	B12
9 139 084	5344	157	5521	110	4.43	0.27	4.68	0.15	0.05	0.14	0.01	0.15	H14
9 161 068	5023	128	5120	80	3.23	0.28	3.26	0.10	−0.36	0.18	−0.29	0.15	T12
9 166 700	6310	66	6318	187	4.15	0.11	4.20	0.20	−0.17	0.13	−0.10	0.45	W13
9 206 432	6415	86	6608	60	4.11	0.11	4.23	0.03	−0.01	0.12	0.23	0.06	B12
9 226 926	6663	207	6580	142	4.11	0.11	4.12	0.21	−0.16	0.13	−0.15	0.22	M13
9 273 312	3963	130	3900	50	1.77	0.19	...	...	−0.09	0.13	...	...	Ma12
9 286 638	7015	75	6900	200	4.01	0.16	3.90	0.10	−0.08	0.12	−0.01	0.14	N14
9 289 275	6109	90	5931	73	4.09	0.14	4.25	0.12	0.08	0.12	0.07	0.12	M13
9 350 124	4037	115	4070	50	1.86	0.19	...	...	−0.02	0.12	...	...	Ma12
9 408 694	7051	99	6810	136	3.90	0.16	3.80	0.15	0.08	0.15	−0.08	0.15	H14
9 413 057	8547	212	8588	97	3.90	0.12	3.59	0.05	−0.16	0.13	−0.56	0.15	Tk12
9 425 139	5695	117	5741	114	4.21	0.19	4.37	0.15	0.22	0.15	0.45	0.15	H14
9 451 706	5974	103	6149	52	4.14	0.14	4.33	0.10	0.11	0.11	0.28	0.08	Bu12
9 474 021	4244	140	4080	80	1.94	0.28	1.20	0.10	−0.28	0.14	−0.47	0.15	T12
9 478 990	6279	103	6260	125	4.11	0.12	4.10	0.15	−0.08	0.14	−0.29	0.15	H14
9 491 832	5805	82	5820	116	4.10	0.15	4.15	0.15	0.21	0.14	0.31	0.15	H14
9 512 063	5889	84	5882	85	4.14	0.15	4.14	0.12	−0.25	0.15	−0.19	0.16	M13
9 527 334	5854	76	5923	118	4.26	0.11	4.59	0.15	−0.05	0.17	0.12	0.15	H14
9 527 915	5106	121	5221	104	4.54	0.26	4.35	0.15	−0.02	0.17	−0.15	0.15	H14
9 528 112	3141	69	3000	20	0.40	0.15	...	...	−0.99	0.11	...	...	Ma12
9 532 030	4454	77	4472	56	2.52	0.16	2.35	0.12	−0.02	0.11	−0.11	0.10	M13
9 532 903	4984	94	5066	150	2.70	0.20	3.02	0.15	−0.09	0.14	0.09	0.10	M14
9 534 041	4945	94	5061	63	2.57	0.19	3.10	0.14	−0.19	0.15	0.02	0.10	M13
9 549 648	6219	95	6164	123	4.00	0.13	4.38	0.15	−0.04	0.15	−0.07	0.15	H14
9 573 539	5641	120	5705	50	4.39	0.15	4.64	0.10	0.09	0.14	0.07	0.08	Bu12
9 592 705	6123	79	6082	55	4.05	0.12	3.98	0.10	0.09	0.11	0.15	0.08	Bu12
9 593 633	3723	78	3700	70	1.39	0.20	...	...	−0.06	0.13	...	...	Ma12
9 594 857	7199	248	7000	0	3.76	0.15	...	...	0.16	0.11	...	...	M14
9 597 345	5276	237	5502	110	3.92	0.41	4.39	0.15	0.11	0.14	0.37	0.15	H14
9 631 995	5869	80	5852	117	4.22	0.14	4.32	0.15	0.04	0.16	0.19	0.15	H14
9 632 503	4074	115	3960	60	1.91	0.18	...	...	−0.07	0.12	...	...	Ma12
9 641 031	6104	114	6152	195	4.14	0.13	3.99	0.14	−0.09	0.19	−0.20	0.14	M07
9 651 065	7313	156	7010	140	3.93	0.13	3.82	0.15	0.05	0.15	−0.09	0.15	H14
9 655 114	7484	161	7400	148	3.87	0.12	3.90	0.15	−0.02	0.13	0.03	0.15	H14
9 655 167	5017	73	5036	82	2.72	0.16	3.03	0.17	−0.04	0.12	−0.01	0.10	M13
9 656 348	7803	79	7177	155	3.94	0.12	3.91	0.21	−0.13	0.11	0.10	0.14	H14
9 663 113	6122	93	5816	180	4.04	0.13	3.80	0.10	0.06	0.12	−0.20	0.35	W13
9 696 358	6090	96	6131	75	4.07	0.12	...	...	0.07	0.12	0.13	0.10	H13
9 700 322	6977	218	6700	134	4.00	0.14	3.70	0.15	0.04	0.14	0.17	0.15	H14
9 700 679	5717	246	5176	140	3.83	0.44	3.37	0.26	0.08	0.13	0.04	0.12	M13
9 714 702	4849	73	4641	0	2.55	0.13	1.64	0.00	−0.17	0.13	−0.36	0.08	P09
9 715 099	6153	66	6180	58	4.05	0.12	4.07	0.11	0.06	0.11	0.07	0.12	M13
9 716 090	5008	76	5053	78	2.72	0.16	3.17	0.15	−0.04	0.13	0.02	0.10	M13
9 716 220	7504	178	7600	0	3.86	0.12	...	...	−0.03	0.13	...	...	M14
9 716 522	4893	76	4860	57	2.62	0.13	2.82	0.11	−0.05	0.11	−0.03	0.10	M13
9 716 667	7747	153	7600	0	3.91	0.12	...	...	−0.12	0.11	...	...	M14
9 717 943	5837	76	5967	119	4.09	0.15	4.30	0.15	0.13	0.12	0.16	0.15	H14
9 775 454	7255	87	7109	159	3.92	0.14	3.91	0.21	0.14	0.13	...	...	H98
9 776 739	4981	97	4922	150	2.67	0.17	2.81	0.15	−0.03	0.12	0.03	0.10	M14
9 777 532	7335	207	7300	0	3.89	0.13	...	...	0.02	0.14	...	...	M14

Table A.2. continued.

KIC	$T_{\rm eff}^{\rm LAM}$ (K)	err	$T_{\rm eff}^{\rm Lit}$ (K)	err	$\log g^{\rm LAM}$ (dex)	err	$\log g^{\rm Lit}$ (dex)	err	$[{\rm Fe/H}]^{\rm LAM}$ (dex)	err	$[{\rm Fe/H}]^{\rm Lit}$ (dex)	err	Reference
9 818 381	5829	75	6074	50	4.14	0.14	4.59	0.10	0.14	0.11	0.43	0.08	Bu12
9 836 959	5860	73	5853	117	4.25	0.13	4.34	0.15	−0.30	0.14	−0.21	0.15	H14
9 838 331	3900	83	3840	60	1.70	0.17	...	...	−0.02	0.11	...	...	Ma12
9 872 165	4313	112	4030	50	2.16	0.24	...	...	−0.10	0.12	...	...	Ma12
9 873 254	5420	161	5677	113	4.15	0.29	4.39	0.15	0.08	0.13	0.49	0.15	H14
9 881 662	5998	83	6206	124	4.17	0.13	4.60	0.15	−0.06	0.14	0.13	0.15	H14
9 884 104	5720	79	5788	115	4.18	0.14	4.24	0.15	0.25	0.12	0.40	0.15	H14
9 895 798	3469	72	3868	120	0.97	0.17	1.71	0.00	−0.05	0.10	−0.06	0.00	M14
9 896 545	3302	87	3320	100	0.50	0.16	...	...	−0.12	0.13	...	...	Ma12
9 950 612	4472	283	4689	93	4.61	0.12	4.73	0.15	−0.13	0.12	−0.05	0.15	H14
9 955 598	5388	171	5410	60	4.46	0.20	4.48	0.03	0.12	0.16	0.11	0.06	B12
9 963 100	3793	109	3600	80	1.36	0.26	...	...	−0.16	0.13	...	...	Ma12
9 964 614	19 364	982	20 300	0	3.77	0.11	3.90	0.00	−0.02	0.10	...	...	Ba11
10 016 239	6418	85	6340	60	4.12	0.11	4.31	0.03	−0.00	0.13	−0.05	0.06	B12
10 018 963	6341	177	6020	60	4.10	0.18	3.95	0.03	−0.20	0.22	−0.35	0.06	B12
10 026 544	6382	127	6149	122	4.12	0.12	3.79	0.15	−0.26	0.13	−0.42	0.15	H14
10 055 126	5848	89	5905	118	4.18	0.14	4.36	0.15	−0.23	0.17	−0.09	0.15	H14
10 073 601	7043	126	6680	133	3.76	0.17	3.47	0.15	0.22	0.12	−0.26	0.15	H14
10 079 226	5855	94	5854	65	4.21	0.13	4.27	0.11	0.10	0.12	0.10	0.11	M13
10 122 402	3855	93	3770	80	1.60	0.19	...	...	−0.03	0.11	...	...	Ma12
10 129 425	4036	120	3900	40	4.64	0.14	...	...	−0.27	0.12	...	...	Ma12
10 130 039	5860	67	5828	116	4.27	0.11	4.42	0.15	0.00	0.12	−0.08	0.15	H14
10 130 954	18 972	988	19 400	0	3.77	0.12	4.00	0.00	−0.03	0.11	...	...	Ba11
10 136 549	5797	82	5683	113	4.15	0.18	4.13	0.15	0.07	0.12	0.02	0.15	H14
10 140 513	5933	76	6030	120	4.14	0.13	4.30	0.15	−0.04	0.15	−0.52	0.15	H14
10 186 608	4714	87	4725	80	2.62	0.14	2.43	0.10	−0.06	0.12	0.00	0.15	T12
10 187 017	5035	118	4903	74	4.62	0.12	4.61	0.03	0.04	0.18	0.08	0.07	Ma14
10 187 831	7468	161	7100	200	3.87	0.14	3.00	0.50	0.03	0.15	...	...	C10
10 257 435	3948	98	3960	60	1.75	0.19	...	...	−0.02	0.12	...	...	Ma12
10 273 960	6525	83	6460	129	4.11	0.11	4.13	0.15	−0.05	0.12	−0.13	0.15	H14
10 285 114	16 278	753	18 200	0	3.78	0.11	4.40	0.00	−0.02	0.11	...	...	Ba11
10 318 874	4516	264	4610	52	4.58	0.13	4.38	0.10	−0.01	0.17	0.29	0.08	Bu12
10 319 385	5663	93	5697	113	4.33	0.15	4.60	0.15	0.16	0.14	0.25	0.15	H14
10 388 249	4607	96	4743	57	2.60	0.13	2.87	0.12	−0.04	0.12	0.00	0.10	M13
10 426 854	5048	174	4955	80	2.73	0.42	2.50	0.10	−0.45	0.20	−0.37	0.15	T12
10 536 147	20 400	1098	20 800	416	3.78	0.11	3.80	0.15	−0.03	0.10	−0.15	0.15	H14
10 586 004	5746	66	5776	50	4.22	0.13	4.18	0.10	0.16	0.11	0.31	0.08	Bu12
10 593 626	5671	99	5518	44	4.39	0.14	4.44	0.06	0.01	0.15	−0.29	0.06	Bu12
10 604 429	7335	148	7200	200	3.85	0.15	3.50	0.50	0.09	0.13	...	...	C10
10 619 192	5511	178	5787	54	4.06	0.26	4.72	0.10	−0.00	0.15	0.41	0.08	Bu12
10 658 302	16 436	1099	15 900	318	3.78	0.11	3.90	0.15	−0.02	0.13	−0.17	0.15	H14
10 663 892	5848	73	6020	120	4.27	0.12	4.90	0.15	−0.35	0.14	−0.08	0.30	H14
10 722 485	5842	65	5681	113	4.24	0.12	4.36	0.15	−0.30	0.15	−0.27	0.15	H14
10 794 087	5771	76	5721	114	4.20	0.13	3.91	0.15	0.17	0.12	0.25	0.15	H14
10 801 138	4031	96	4130	40	1.83	0.14	...	...	−0.07	0.11	...	...	Ma12
10 801 273	4389	249	3970	60	4.29	0.61	...	...	−0.10	0.16	...	...	Ma12
10 850 327	5938	73	6022	190	4.17	0.15	4.10	0.25	−0.23	0.14	−0.40	0.50	W13
10 917 433	5795	67	5680	0	4.29	0.11	4.33	0.00	0.07	0.12	...	...	P13
10 923 629	6197	91	6214	60	3.96	0.11	3.82	0.03	0.07	0.12	0.16	0.06	B12
10 960 750	19 591	832	19 960	880	3.75	0.11	3.91	0.11	−0.01	0.10	−0.04	0.16	L11
11 027 624	5937	75	5865	117	4.11	0.12	3.96	0.15	0.07	0.12	0.06	0.15	H14
11 074 541	5062	136	4869	97	4.60	0.13	4.44	0.15	0.07	0.15	−0.09	0.15	H14
11 075 279	5457	110	5649	112	4.39	0.15	4.57	0.15	0.12	0.13	0.33	0.15	H14
11 075 737	5796	97	5804	116	4.30	0.13	4.43	0.15	−0.32	0.15	−0.20	0.15	H14
11 081 729	6460	64	6630	60	4.13	0.11	4.25	0.03	−0.16	0.14	−0.12	0.06	B12
11 086 270	5941	130	5960	0	4.16	0.17	4.37	0.00	−0.20	0.16	...	...	P13
11 133 306	5877	76	5982	82	4.27	0.12	...	...	−0.07	0.15	−0.02	0.10	H13
11 137 075	5604	166	5590	60	4.00	0.31	4.01	0.03	−0.03	0.18	−0.06	0.06	B12
11 192 141	4210	98	4204	84	2.06	0.16	2.13	0.15	−0.02	0.12	−0.12	0.15	H14
11 197 047	3857	104	3700	80	1.44	0.25	...	...	−0.15	0.13	...	...	Ma12

Table A.2. continued.

KIC	$T_{\rm eff}^{\rm LAM}$ (K)	err	$T_{\rm eff}^{\rm Lit}$ (K)	err	$\log g^{\rm LAM}$ (dex)	err	$\log g^{\rm Lit}$ (dex)	err	$[{\rm Fe/H}]^{\rm LAM}$ (dex)	err	$[{\rm Fe/H}]^{\rm Lit}$ (dex)	err	Reference
11 241 912	5889	124	5931	118	4.20	0.14	4.40	0.15	−0.05	0.20	−0.06	0.15	H14
11 244 118	5721	112	5745	60	4.17	0.14	4.09	0.03	0.20	0.12	0.35	0.06	B12
11 244 265	3807	110	3650	70	1.59	0.17	...	...	−0.16	0.13	...	...	Ma12
11 245 491	3498	123	3330	90	0.79	0.36	...	...	−0.13	0.12	...	...	Ma12
11 253 711	5883	102	5816	0	4.22	0.15	4.48	0.00	−0.32	0.17	...	...	P13
11 336 883	6189	72	6332	126	4.14	0.12	4.35	0.15	0.01	0.12	0.08	0.15	H14
11 342 694	4443	81	4575	80	2.67	0.17	2.82	0.10	0.13	0.12	0.38	0.15	T12
11 359 879	5756	88	5515	110	4.17	0.15	4.46	0.15	0.21	0.14	0.36	0.15	H14
11 360 704	19 005	871	20 700	0	3.75	0.12	4.10	0.00	−0.03	0.11	...	...	Ba11
11 392 618	5742	76	5710	41	4.27	0.12	4.28	0.04	0.07	0.12	0.01	0.03	W13
11 395 018	5619	149	5740	114	4.14	0.27	3.65	0.15	0.17	0.12	0.02	0.15	H14
11 444 313	4705	76	4750	80	2.61	0.13	2.46	0.10	−0.01	0.11	−0.01	0.15	T12
11 445 774	6214	72	6210	124	4.18	0.11	4.60	0.15	−0.13	0.13	−0.20	0.15	H14
11 446 443	5804	77	5874	65	4.32	0.15	4.47	0.02	0.05	0.15	−0.01	0.08	To12
11 448 266	5890	85	6110	122	4.23	0.13	4.70	0.15	−0.12	0.16	−0.04	0.15	H14
11 499 354	5817	79	6020	120	4.24	0.13	4.39	0.15	0.02	0.17	0.13	0.15	H14
11 512 246	5977	120	5828	100	4.14	0.15	...	...	−0.12	0.16	−0.05	0.10	H13
11 551 692	5018	119	4977	99	4.61	0.12	4.72	0.15	0.07	0.13	0.11	0.15	H14
11 554 435	5473	107	5675	113	4.46	0.18	4.74	0.15	0.07	0.12	0.14	0.15	H14
11 560 897	5881	90	5831	116	4.18	0.14	4.27	0.15	−0.07	0.17	0.11	0.15	H14
11 567 375	4368	110	4030	50	2.18	0.24	...	...	−0.43	0.15	...	...	Ma12
11 569 659	4934	116	4890	80	2.57	0.18	2.43	0.10	−0.34	0.15	−0.27	0.15	T12
11 621 223	5907	107	6134	122	4.10	0.13	4.50	0.15	0.10	0.12	0.22	0.15	H14
11 623 629	5706	100	5564	111	4.25	0.14	4.52	0.15	0.03	0.17	−0.14	0.15	H14
11 653 958	6454	58	6450	129	4.08	0.11	4.20	0.15	−0.04	0.13	−0.20	0.15	H14
11 654 210	5947	83	6200	124	4.19	0.12	4.63	0.15	−0.22	0.14	0.12	0.15	H14
11 657 684	4850	72	4840	80	2.55	0.13	2.44	0.10	−0.17	0.12	−0.09	0.15	T12
11 717 120	5400	262	5150	60	3.92	0.39	3.68	0.03	−0.38	0.17	−0.30	0.06	B12
11 766 491	3893	81	3880	80	1.72	0.15	...	...	−0.02	0.11	...	...	Ma12
11 771 430	5742	75	5849	116	4.13	0.17	4.23	0.15	0.05	0.13	0.26	0.15	H14
11 774 991	4824	237	4710	94	4.26	0.52	4.62	0.15	0.08	0.13	0.08	0.15	H14
11 807 274	6185	84	6058	52	4.09	0.12	3.91	0.10	−0.16	0.15	−0.12	0.08	Bu12
11 817 929	13 467	903	16 000	0	3.84	0.16	3.70	0.00	0.10	0.11	...	...	Ba11
11 853 905	5798	66	5857	120	4.26	0.11	4.25	0.10	0.12	0.12	0.17	0.06	Bu12
11 857 884	3450	76	3440	110	0.79	0.24	...	...	−0.05	0.11	...	...	Ma12
11 904 151	5760	72	5643	75	4.32	0.13	4.34	0.01	0.06	0.13	−0.15	0.07	To12
11 973 705	12 137	1120	11 150	223	4.03	0.13	4.00	0.15	0.06	0.15	0.15	0.15	H14
12 009 504	6075	79	6065	60	4.10	0.11	4.21	0.03	−0.03	0.15	−0.09	0.06	B12
12 068 975	6161	122	6004	102	4.18	0.12	...	...	−0.33	0.18	−0.38	0.10	H13
12 105 051	5213	128	5376	107	4.30	0.38	4.55	0.15	0.07	0.11	0.38	0.15	H14
12 107 021	5944	69	6104	122	4.20	0.13	4.52	0.15	−0.19	0.14	−0.01	0.15	H14
12 258 330	16 203	1006	14 700	200	3.77	0.11	3.85	0.04	−0.00	0.11	−0.30	0.16	L11
12 301 181	5116	144	4997	99	4.61	0.12	4.60	0.15	0.07	0.13	−0.01	0.15	H14
12 454 461	5949	119	6048	120	4.18	0.16	4.31	0.15	0.04	0.16	0.13	0.15	H14
12 737 015	5978	92	6045	120	4.13	0.13	4.15	0.15	0.06	0.13	0.16	0.15	H14

Table A.3. Stellar parameters for the whole sample of LAMOST spectra.

Spectrum	HJD (−2 450 000)	KIC	Designation	S/N$_r$	RA °	DEC °	*SpT*	$T_{\rm eff}$ (K)	err	log *g* dex	err	[Fe/H] dex	err	*RV* (km s^{-1})	err	$v \sin i$	err	P(χ^2)
spec-56083-IF04_B56083_sp12-240.fits	6083.2758	1 002 134	J194236.51+465436.2	52	295.6521606	46.9100761	K0II	4762	98	2.74	0.17	-0.01	0.12	0.2	19.4	< 120	0	...
spec-56083-IF04_B56083_sp11-028.fits	6083.2758	1 008 415	J194104.02+470135.0	110	295.2667847	47.0263977	K2III	4619	79	2.64	0.13	0.12	0.11	-6.5	17.8	< 120	0	...
spec-56083-IF04_B56083_sp11-209.fits	6083.2758	1 014 763	J193708.62+470632.9	23	294.2859192	47.1091385	F2V	6110	101	4.07	0.12	0.03	0.13	-23.9	24.1	< 120	0	...
spec-56083-IF04_B56083_sp11-210.fits	6083.2758	1 014 871	J193837.77+470814.8	56	294.6574097	47.1374626	M3III	3531	87	1.09	0.12	-0.05	0.10	-56.8	55.9	< 120	0	...
spec-56094-kepler05F56094_sp01-243.fits	6094.2989	1 023 665	J192153.09+364634.8	20	290.4712219	36.7763596	F8	5914	264	4.09	0.16	-0.54	0.31	-35.5	31.2	< 120	0	...
spec-56094-kepler05B56094_sp01-243.fits	6094.2131	1 023 745	J192158.43+364638.9	50	290.4934692	36.7774773	K2III	4471	92	2.37	0.16	-0.17	0.13	28.7	18.1	< 120	0	...
spec-56094-kepler05B56094_2_sp01-243.fits	6094.2537	1 023 848	J192205.31+364715.1	51	290.5221558	36.7875481	K3III	4466	100	2.41	0.20	-0.01	0.11	-122.3	18.1	< 120	0	...
spec-56094-kepler05B56094_2_sp01-207.fits	6094.2537	1 024 114	J192221.97+364643.2	63	290.5915527	36.7786751	K1III	4800	123	2.91	0.27	-0.12	0.15	-94.5	18.2	< 120	0	...
spec-56094-kepler05F56094_sp01-212.fits	6094.2989	1 024 464	J192240.76+364638.6	12	290.6698608	36.7773972	K3V	4308	228	2.43	0.55	-0.11	0.18	-5.8	69.3	328	78	...
spec-56094-kepler05B56094_sp01-219.fits	6094.2131	1 024 986	J192308.20+364527.1	277	290.7842102	36.7575302	K4III	4266	103	2.08	0.14	-0.06	0.11	-15.7	17.3	< 120	0	...
...	...	...	...	...	...	...	...	...	...	...	...	...	...	...	...	...	...	...
spec-56930-KP192323N501616V03_sp07-169.fits	6930.0216	10 920 086	J192724.49+481910.4	111	291.8520830	48.3195560	F6V	6439	57	4.12	0.11	-0.03	0.13	-35.9	18.3	< 120	0	0.0025
...	...	...	...	...	...	...	...	...	...	...	...	...	...	...	...	...	...	...
spec-56918-KP192323N501616V_sp07-152.fits	6918.0333	10 920 130	J192729.65+482148.4	96	291.8735830	48.3634720	K1.5III	4655	92	2.60	0.14	-0.03	0.11	4.7	18.3	< 120	0	0.8880
...	...	...	...	...	...	...	...	...	...	...	...	...	...	...	...	...	...	...

Table A.4. Activity indicators.

Spectrum	HJD (−2 450 000)	KIC	RA °	DEC °	$EW^{\rm res}_{\rm H\alpha}$ (Å)	err	$EW^{\rm res}_{8498}$ (Å)	err	$EW^{\rm res}_{8542}$ (Å)	err	$EW^{\rm res}_{8662}$ (Å)	err	Notes*	$P_{\rm rot}$ (days)	Ref.**
spec-55712-IF10M_sp02-195.fits	5712.29462	3 725 427	283.916107	38.864498	1.76	0.59	...	...	0.30	0.30	0.83	0.30	E	...	...
spec-55712-IF10M_sp03-059.fits	5712.29449	5 079 590	284.472107	40.213600	2.54	0.50	...	...	1.20	0.59	0.57	0.59	E	2.016	R13
spec-55712-IF10M_sp03-123.fits	5712.29447	5 342 618	284.399689	40.573399	3.26	0.38	0.87	0.35	1.77	0.36	1.09	0.36	E	...	...
...	...	...	...	...	...	...	...	...	...	...	...	...	...	...	...
spec-56583-KP195920N454621V03_sp02-053.fits	6582.98089	8 257 776	299.115295	44.175140	1.45	0.59	0.66	0.47	2.04	0.49	1.49	0.49	N	...	...
spec-56561-KP195920N454621V01_sp01-083.fits	6561.00326	7 919 763	299.962458	43.693778	1.06	0.25	0.51	0.32	0.63	0.33	0.78	0.33		3.784	Mc14
spec-56561-KP195920N454621V01_sp14-048.fits	6561.00263	9 293 772	296.611792	45.792369	1.11	0.35	0.19	0.44	...	...	0.62	0.46	D	...	...
...	...	...	...	...	...	...	...	...	...	...	...	...	...	...	...
...	...	...	...	...	...	...	...	...	...	...	...	...	...	...	...

Notes. (*) E = Hα emission above the continuum; N = [N II] nebular lines; D = Doubtful Hα core filling. (**) D11 = Debosscher et al. (2011); N13 = Nielsen et al. (2013); R13 = Reinhold et al. (2013); Mc13 = McQuillan et al. (2013); Mc14 = McQuillan et al. (2014); M15 = Mazeh et al. (2015).

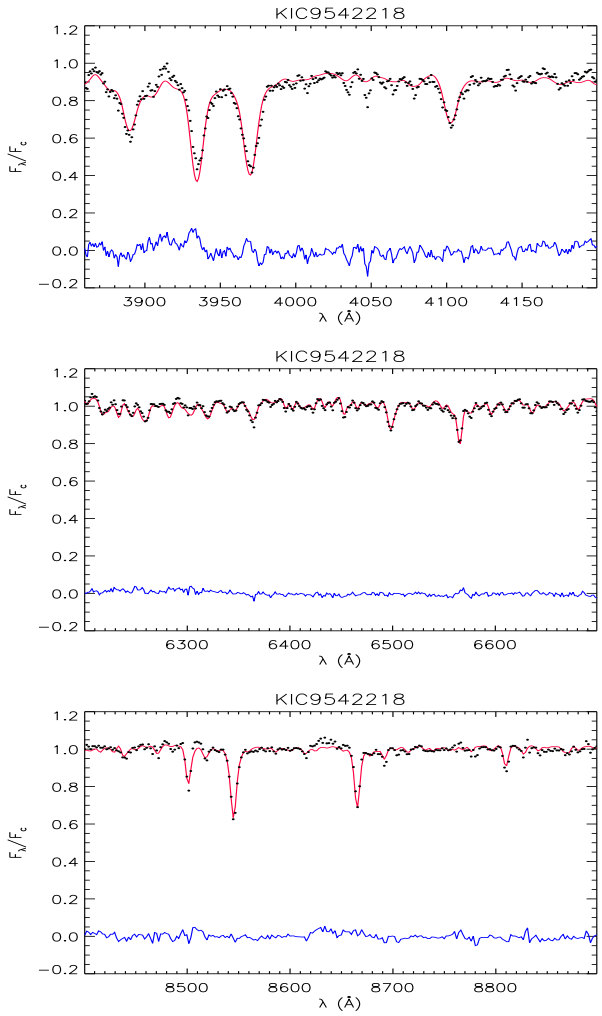

Fig. B.1. Example of the continuum-normalized LAMOST spectrum of KIC 9542218 in three spectral regions (dots). The best template found by ROTFIT for each spectral region is overplotted with a thin red line. The difference between the two spectra is shown in the bottom of each panel with a blue full line. We note the large residual of the fit in the first region where a mid-F type template (HD 150453) is not able to reproduce either the Balmer lines or narrower absorptions, such as the Fe I λ 4057 Å lines. The spectrum at red wavelengths is instead well reproduced by a cool giant template.

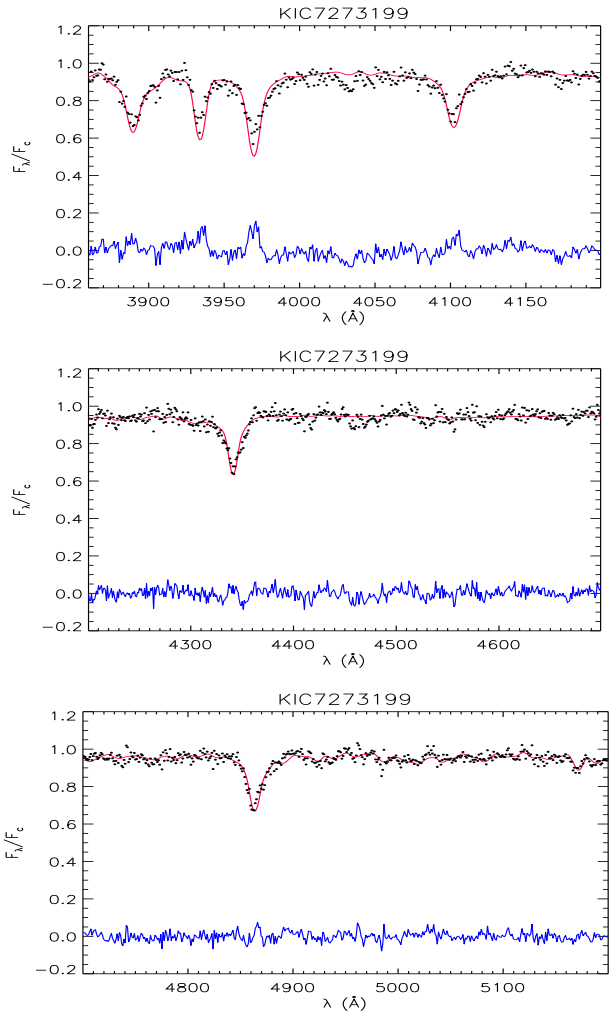

Fig. B.2. Example of the continuum-normalized LAMOST spectrum of KIC 7273199 in three spectral regions (dots). The best template found by ROTFIT for each spectral region is overplotted with a thin red line. The difference between the two spectra is shown in the bottom of each panel with a blue full line. The spectrum is clearly reminiscent of a warm (F-type) star. However, the asymmetry in the red wings of the Balmer Hγ and Hβ lines, can be due to a spectroscopic companion.

Appendix B: Stars with discrepant $T_{\rm eff}$ and log g compared to APOKASC and SAGA

The two stars with very discrepant $T_{\rm eff}$ and $\log g$ values, compared with those listed in the APOKASC catalog, are KIC 9542218 and KIC 8936084 from left to right of Fig. 6a, respectively. KIC 8936084, although correctly classified as K1 III, displays very broad spectral features, which have been fitted by our code in most of the analyzed spectral segments with a giant star template with a $v \sin i \simeq 205$ km s^{-1}. We cannot exclude that the large $v \sin i$ is instead the effect of an unresolved SB. The values of $T_{\rm eff}$ and $\log g$ and their errors are affected by those of main-sequence templates that have been selected together with giant star templates, particularly in some spectral regions. We think that this is the result of the large line broadening or binarity. The other discrepant star, KIC 9542218, is the most interesting case because its spectrum shows clear signatures of a hot star (Balmer Hδ, Hϵ and H$_8$ lines) superimposed on a cool star in the bluest spectral segment (3850–4200 Å), while it is reminiscent of a normal red giant in the red part of the spectrum (see Fig. B.1). This explains why the LAMOST $T_{\rm eff}$ and $\log g$ values are higher than those in the APOKASC catalog. The contribution of the hot component could be so small in the near-IR to make it undetectable with APOGEE, but the observed near-IR spectrum of this star could be still slightly contaminated and the parameters reported in the APOKASC catalog could have been affected. The large wavelength coverage of the LAMOST from the near UV to the near-IR is suitable to detect composite spectra with very different stars.

Four stars appear as outliers in Fig. 7. The most noticeable case is that of KIC 7273199, which displays very discrepant values for all the parameters. We found a temperature $T_{\rm eff} = 6190$ K and a metallicity [Fe/H] = −2.05 dex, while the SAGA catalog reports 4917 K and −0.59 dex, respectively. The spectrum of this star, which is reminiscent of a warm (F-type) star, shows asymmetries in the wings of the Balmer Hγ and Hβ lines that can be due to a spectroscopic companion. This could have given rise to this large discrepancy of atmospheric parameters derived with very different methods and suggests to consider them as highly unreliable. KIC 5373233 and KIC 8212479 display strong discrepancies only for $\log g$, given our values of 3.6 ± 0.5 and

3.4 ± 0.5 dex for the two stars, respectively, i.e., more than 1 dex higher than the values of SAGA that are more typical of giant stars. The former star is a fast rotator ($v \sin i \simeq 220\,\mathrm{km\,s^{-1}}$), which can explain a rather inaccurate value. The second star has instead a projected rotation velocity that is not detectable with the LAMOST resolution ($v \sin i \leq 120\,\mathrm{km\,s^{-1}}$). The last object, KIC 8145677, has both $\log g$ and [Fe/H] that is much different than the SAGA values. The latter catalog reports a gravity $\log g = 2.41$ and a metallicity [Fe/H] $= -1.77$ dex. The LAMOST spectrum (see Fig. B.3), however, does not seem that of a very metal poor star, but it rather resembles a mildly metal poor giant or subgiant, in agreement with the value of [Fe/H] $= -0.53$ that we found.

Appendix C: Continuum surface fluxes as a function of atmospheric parameters

The continuum flux at 6563 Å (Hα center) and in the centers of the Ca II-IRT lines as a function of the APs ($T_{\rm eff}$,$\log g$, and [Fe/H]) was measured in the NextGen synthetic spectra. We took the average continuum flux in two regions at the two sides of the aforementioned lines. We plot the continuum flux at 6563 Å as a function of $T_{\rm eff}$ for different values of $\log g$ and [Fe/H] in Fig. C.1. The continuum flux at the line center of the Ca II λ 8542 Å line, F_{8542}, is shown in Fig. C.2. It is worth noticing that the dependence of these continuum fluxes on $\log g$ and [Fe/H] is negligible for $T_{\rm eff} \geq 4000$ K. The flux differences as a function of $\log g$ are more pronounced at lower temperatures, mostly when $T_{\rm eff} \leq 3500$ K, which is likely due to the strengthening of molecular bands. Anyway, this dependence is a second-order effect, compared to the $T_{\rm eff}$ dependence, and it is properly taken into account when we convert the EWs into line fluxes using the $\log g$ and [Fe/H] values that we derived, although their accuracy is not as high as that of $T_{\rm eff}$ determinations.

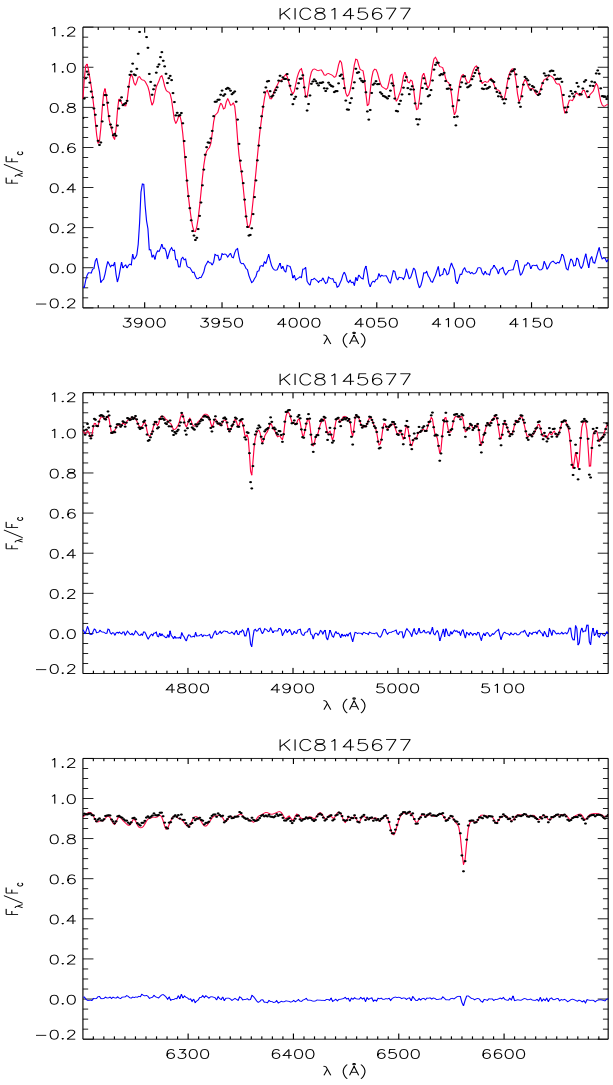

Fig. B.3. Example of the continuum-normalized LAMOST spectrum of KIC 8145677 in three spectral regions (dots). The best template found by ROTFIT for each spectral region is overplotted with a thin red line. The difference between the two spectra is indicated in the bottom of each panel with a blue full line.

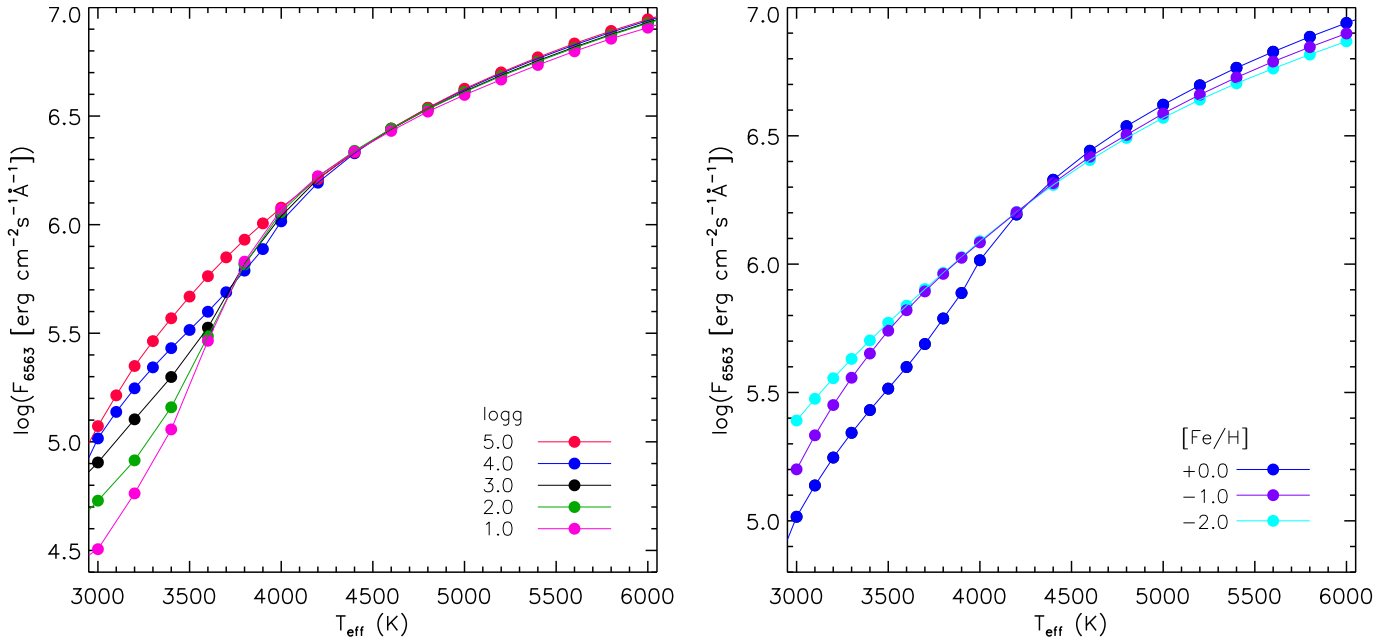

Fig. C.1. *Left panel*: continuum flux at the Hα wavelength, as derived from the NextGen spectra for a solar metallicity, vs. $T_{\rm eff}$. Different $\log g$ are coded with different colors. *Right panel*: the same continuum flux at $\log g = 4.0$ for three values of metallicity.

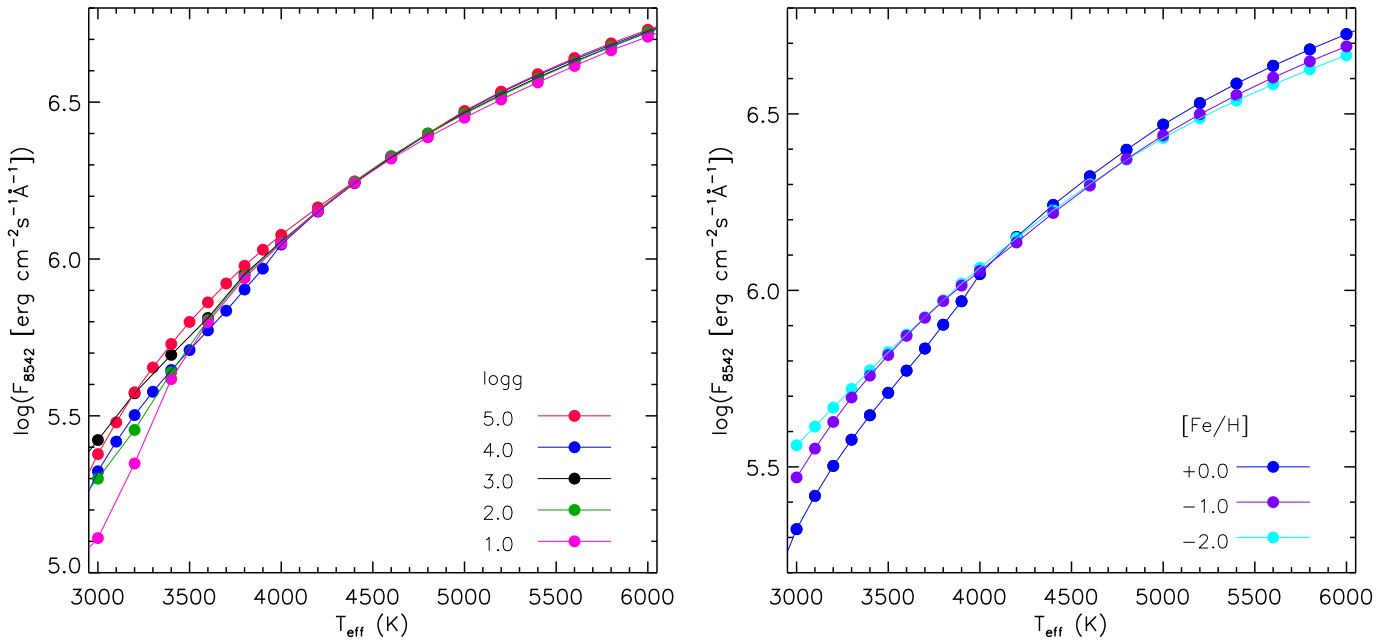

Fig. C.2. Same as Fig. C.1 for the continuum flux at the Ca II-IRT wavelengths.